The International Journal of Advanced Manufacturing Technology (2025) 136:5305–5334
https://doi.org/10.1007/s00170-025-15107-8

ORIGINAL ARTICLE

Geometrical characterization of circular multi-layered CMT WAAM specimens by 3D structured light scanning

Jacopo Lettori[1] · Cesare Esposto[1] · Margherita Peruzzini[2] · Marcello Pellicciari[3] · Roberto Raffaeli[3]

Received: 23 October 2024 / Accepted: 23 January 2025 / Published online: 11 February 2025

Abstract

To ensure the geometric accuracy of wire arc additive manufacturing (WAAM) components, it is essential to analyze how process parameters influence the weld bead dimensions and shape. This paper presents a formal and repeatable procedure to entirely characterize the geometry of beads by enhanced full-coverage optical scanning with focus on multi-layered thin-walled closed specimens realized by the cold metal transfer (CMT) welding process. A series of circular specimens have been manufactured according to a DOE plan of process parameters, scanned with a GOM fringe projection 3D optical scanner, geometrically processed in the Rhinoceros 3D CAD environment, and analyzed by statistical indices according to the ANOVA approach. Average dimensions, lateral surface waviness, interaction between successive layers, and the torch switch-on/off zone of closed layer paths have been assessed. Numerical correlations between bead sizes and deposition parameters have been established. The obtained results also reveal shape and dimensional variability, highlighting the challenges in controlling geometry accuracy. Finally, process planning guidelines are formulated based on such results.

Keywords Wire arc additive manufacturing · Bead geometry analysis · 3D optical scanning · Geometry processing algorithm · Cold metal transfer · Design methods

1 Introduction

Wire arc additive manufacturing (WAAM) is gaining wide interest from academia and the industry [1]. WAAM belongs to the category of directed energy deposition [2] and it consists of an automized welding process where a torch is combined with a robotic solution [3, 4]. Manipulators with five or six DoFs [5], combined to working tables with one or two DoFs [6], are often implemented in WAAM cells. Three different types of welding processes are adopted for WAAM applications [7], namely gas metal arc welding (GMAW) [8], gas tungsten arc welding (GTAW) [9], and plasma arc welding (PAW) [10]. WAAM allows large metal parts to be realized faster than other AM technologies as the deposition rate reaches 5–8 kg/h [5, 11]. Also, multiaxial deposition strategies are permitted thanks to the dexterity of the robot [12], i.e., not constant layer thickness are realized leveraging non-uniform and non-planar slicing approaches [13–15].

In this work, the cold metal transfer (CMT) GMAW is considered being one of the most implemented and efficient technologies for the following reasons. The process, invented by Fronius, is based on a short-circuit welding technique, which reduces spatter and heat input compared to other welding techniques [16, 17]. Fronius welding generators exhibit good capabilities in the modulation of the deposition both in continuous (CMT Continuous, Fig. 1a) and intermittent form (CMT Cycle Step, Fig. 1b) [18, 19]. The CMT Cycle Step can be used in continuous paths to form beads composed of successively deposited drops (Fig. 1b2). Ultimately, this technical choice strongly reduces residual stress and distortions.

Table 1 summarizes the parameters that affect the WAAM deposition, providing a picture on the overall complexity [20]. Some of them are controllable by the user, such as

✉ Roberto Raffaeli
roberto.raffaeli@unimore.it

[1] Department of Engineering "Enzo Ferrari", University of Modena E Reggio Emilia, Via P. Vivarelli 10, 41125 Modena, Italy

[2] Department of Industrial Engineering, Alma Mater Studiorum - University of Bologna, Viale del Risorgimento 2, 40132 Bologna, Italy

[3] Department of Sciences and Methods for Engineering, University of Modena E Reggio Emilia, Via Giovanni Amendola 2, 42122 Modena, Reggio Emilia, Italy

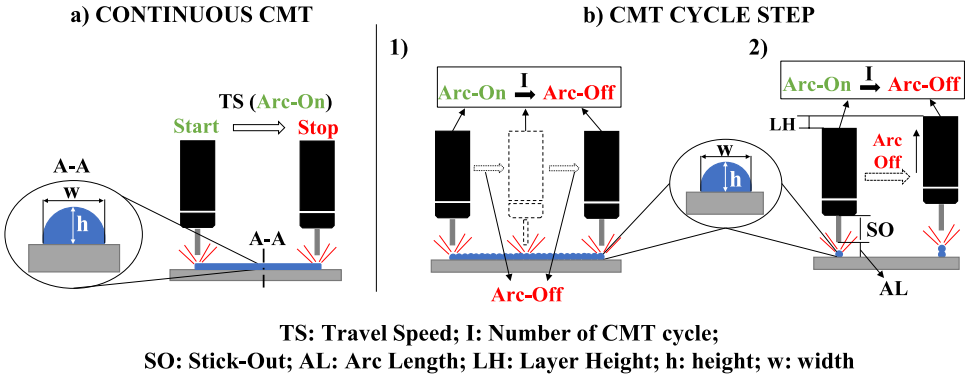

Fig. 1 CMT process parameters in case of **a** continuous and **b** Cycle Step deposition

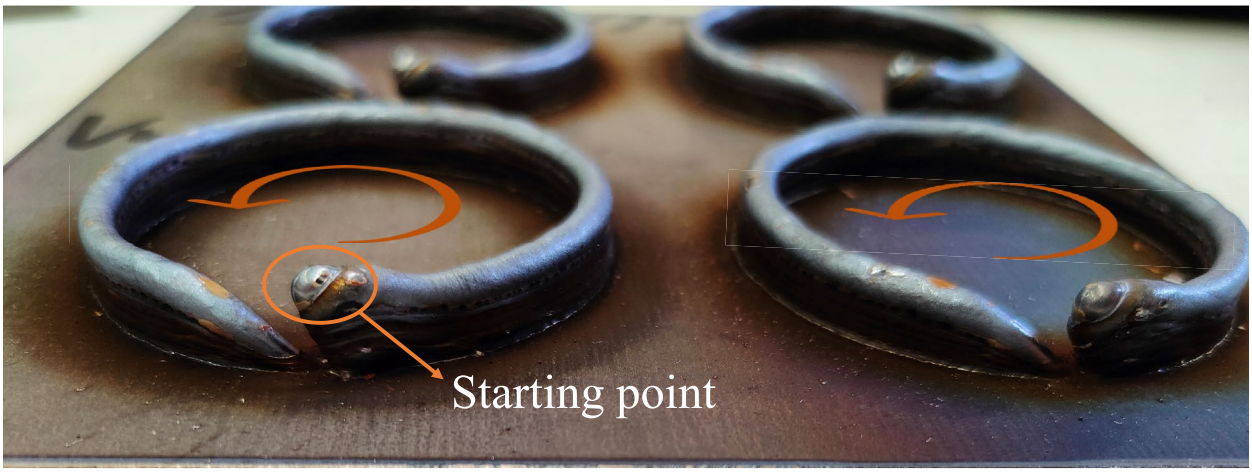

Fig. 2 Printing failure and silicates formation registered in some experiments with low *WFR* and coincident starting positions of successive layers

Table 1 List of the parameters which affect a WAAM process

Welder parameters	Motion parameters	Material and gas parameters
Current [A]	Travel speed [mm/s]	Material composition
Voltage [V]	Type of motion (linear, joint, circular)	Wire diameter [mm]
Wire feed rate [m/min]	Transition function points [mm]	Shielding gas type
Arc length correction factor	Stick out [mm]	
Impulse/dynamic correction factor	Tool angle respect to the gravity direction [°]	
Gas flow rate [l/min]	Tool angle respect to the part surface [°]	
Current ramp [A]	Reachability	
Number of cycle*	Singularities	
Cycle interval number*	Collisions	
Pause interval [s]*		
Polarity		
Start/end parameters		

*Specific for CMT Cycle Step

the wire feed rate (*WFR*), the current level, polarity, the material, the shielding gas type, and flow [21–23]. Other parameters are internally adjusted by the welding source according to mechanisms predefined by the manufacturers. In particular, the heat input modulating voltage and intensity are varied in predefined ranges according to arc formation conditions. Also, Fronius welding sources allow for additional adjustments of these parameters during the start/end welding phases, as these are the most critical intervals of the process [24].

Establishing a clear relationship between welding parameters, heat transfer, and consequent metal transfer [18, 25, 26] is challenging. Furthermore, the motion parameters determine the bead dimensions, namely the Travel Speed (*TS*) and the accelerations imposed on the welding head. They are affected by intrinsic limits of the anthropomorphic robotic system, which include the actual ability to maintain imposed trajectories and speeds [27], reachability, the presence of kinematic singularities, and collision zones. The type of material and the choice of shielding gas further influence the deposition conditions, such as weld bead shape, penetration, and overall quality, further impacting the outcome of the welding process [28]. Heat dissipation is another major factor that influences the geometry assumed by the bead from its transition from liquid to solid, its microstructural properties, and the deformations of the final part. Finally, the geometrical setup, i.e., the distance between the end of the nozzle and the melted substrate, known as stick-out, as well as the tool orientation with respect to the direction of gravity and the slope of the underlying substrate need also to be considered influencing parameters of the obtained bead shape [29].

The control of the process parameters highly determine the shape of the bead and is crucial for a successful material deposition, especially when implementing non-uniform slicing strategies which require the realization of variable bead sizes [14, 28, 30]. Previous works listed in Appendix A (see Table 13) have been done for the geometric characterization of beads as a function of process parameters [31, 32]. They mostly involve single linear beads to evaluate cross-sectional dimensions, i.e., height (h) and width (w), thus attempting the development of predictive models as a function of the studied parameters [33, 34]. In the last years, closed-loop control systems, based on profile measuring systems and temperature sensors, have also been devised to correct the sizes of the bead during the deposition and acting on process parameters in real time, compensating for deviations due to the process [35].

However, dimensions of single-line straight beads are typically obtained from calipers, images of cross-sections or 2D laser sensors, which fails to capture characteristics such as lateral surface waviness, interaction between successive layers, and the torch switch-on/off zone of closed layer paths. The overlap behavior between adjacent and multi-layered beads has been a more limited object of investigation [30]. Few works have focused on the material properties of beads [6] and multi-bead transition walls [36]. These attempts recall the importance of describing the shape of overlapped layers of beads not limiting the assessment on only one bead. None of the analyzed studies reports an approach to define a repeatable procedure of analysis of the quality of the obtained part being the major efforts just limited to the sizes of the generated bead. Knowing the extent of irregularities of the deposited material is of utmost importance for reliable process planning and to guarantee a desired level of geometric accuracy. Besides, rare studies focus on the geometric assessment of multi-layered closed structures that is the typical case in the realization of parts with WAAM [34].

In a nutshell, the following research gaps can be identified from the analysis of the literature:

- Many works focus on the overall size of straight beads, i.e., w or h, while a comprehensive description of the shape is missing, i.e., the surface waviness and the junction zone of closed layer paths.
- Focusing solely on one bead precludes the analysis of the lateral waviness of the sample and the assessment of the surface quality [37].
- The adopted means of measurement, i.e., 2D laser scanner or 2D profilometer, does not allow an assessment of the shape of a series of overlapped beads, since the sides of the lower layers are not reached given the fixed acquisition direction.
- Many studies are related to single bead layer. However, the initial bead deposited on the (often cold) substrate differ from those of subsequent layers [24]. A variable heat dissipation rate is then encountered during the part realization.
- A formalized procedure to identify the influence and the contribution of the single parameter to the shape is missing.

In consideration of such limitations, the paper presents a formalized procedure for the analysis of welding beads based on 3D structured light scanning to achieve a detailed acquisition of the geometry. Unlike in single straight beads, this methodology is applied to closed circular thin-walled specimens, with an emphasis on critical parameters relevant to WAAM, including surface waviness and the discontinuities in the region of layer closure. Such region is critical given that a deposition layer usually consists of at least one outer closed contour and inner ones due to cavities obtained from offsets of the intersection of the geometry with a section surface at a given position, while the remaining area is covered with infill patterns. The last ones are designed to minimize residual stress and induced distortions, also leveraging FEM simulations [38–40].

For this reason, the chosen specimen design is a closed-loop circular path, also allowing the assessment of torch ignition and switch-off zones that determine irregularities in the obtained shape. In fact, the thermal dissipation conditions vary between the start and end of the path, altering material penetration [41]. Lastly, the formation of non-conductive silicates on the surface of the layer can further exacerbate this phenomenon [42] as can be observed in Fig. 2.

Furthermore, the proposed approach leverages high-resolution optical 3D scanning for an accurate description

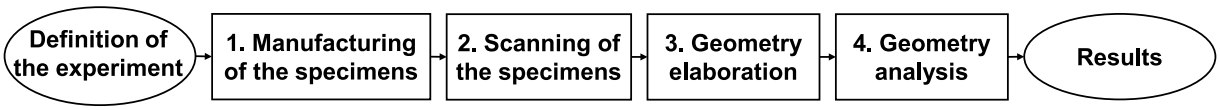

Fig. 3 Workflow of the approach for the bead analysis

of the geometry of circular thin-walled specimens formed by sequentially overlapped layers. By utilizing 3D optical scanners, a comprehensive assessment of the dimensional outcomes and part waviness is allowed, considering the combined effects of multiple layers overlap which are overlooked by online measurement systems that are limited to the acquisition of the profile of the last deposited bead. The adopted 3D acquisition technique further improves the scan of the geometry by integrating multiple viewpoints, ensuring thorough coverage of the entire part. This method exhibits good scalability to different dimensions of specimens or parts to be characterized given the wide range of sizes of the field of view of scanners available on the market, ranging from a few centimeters up to meters. For larger or more complex structures, it is sufficient to adapt the experimental setup to choose the scanner with the most suitable optics and move it all around the part manually or by robotic arms for a complete scan.

As a final goal, the proposed method helps establish a precise and consistent procedure for scanning and predicting the shape of deposited beads relative to the nominal geometry. This allows for a better understanding of how working parameters affect multilayered thin-walled specimens. This approach is beneficial for the choice of optimal allowances and manufacturing tolerances to ensure no material shortage in the areas to be further machined nor excessive metal accumulation elsewhere. Furthermore, the work reports numerical results related to the application of the method to specimens and to the measurement of the variability of the bead sizes, while modulating WFR and TS, also revealing some unexpected behaviors.

The remainder of the paper reports in Sect. 2 on the proposed approach and the experimental campaign. The results obtained are described and statistically analyzed in Sect. 3, providing process planning guidelines from the evidence resulting from the application of the proposed approach. Finally, conclusions and future works are outlined in Sect. 4.

2 Approach for a detailed bead geometry characterization

This section introduces a procedure for bead geometry analysis based on 3D optical scanning, which is consolidated in applications, such as in industry or in the biomedical field, where complex and shaped geometries need to be characterized [43, 44]. The accuracy of modern optical scanning systems is compatible with the specific problem since the measurement errors are at least one order of magnitude inferior to the measured deviations of the bead from the nominal sizes.

The proposed workflow characterizes the deposition by three key aspects: average dimensions, lateral waviness, and irregularities in the torch switch-on/off zones. While this approach is broadly applicable to any WAAM process, the experimental study has focused on the CMT process. The examined parameters include *WFR*, *TS*, and Torch Switch-Off Offset (*TSOO*), which denotes the position of the final path where the torch is switched off.

The approach comprises four phases, depicted in Fig. 3. Initially, the specimens are realized following the definition of a Design of Experiment (DOE) plan [45]. Then, the samples are scanned by an optical 3D fringe projection scanner. Afterward, the obtained geometry is processed with CAD-based algorithms to characterize the shape by numerical indices.

The software tools pipeline to process the acquisitions is reported in Fig. 4. The meshes obtained from the optical scanner are imported into the Rhinoceros 3D® v.7 environment (McNeel Inc.) for the elaboration step. In this context, Grasshopper®, a Rhinoceros 3D® tool for visual programming, automates the geometry analyses. Then, the data obtained with Grasshopper® are plotted using MATLAB® and analyzed with Excel®. The approach has been followed in a preliminary experimental campaign, oriented to the assessment of the validity of the proposed analysis method and to an initial data collection.

2.1 Experimental setup

It is known that DOE is used to plan, execute, and assess controlled tests to optimize a product or process. It involves investigating how input variables, known as factors, impact output variables, i.e., responses. The factors have been identified with the process parameters of the CMT-based WAAM system. At the same time, the response is the geometry of the deposited bead. The experimentation has been developed following the full factorial approach. The characteristics of the adopted experimental apparatus are reported in Table 2.

The experimental setup consists of a WASP 40 × 70 industrial delta 3D printer customized using a Fronius CMT torch as a WAAM tool (Fig. 5). In addition, the printer

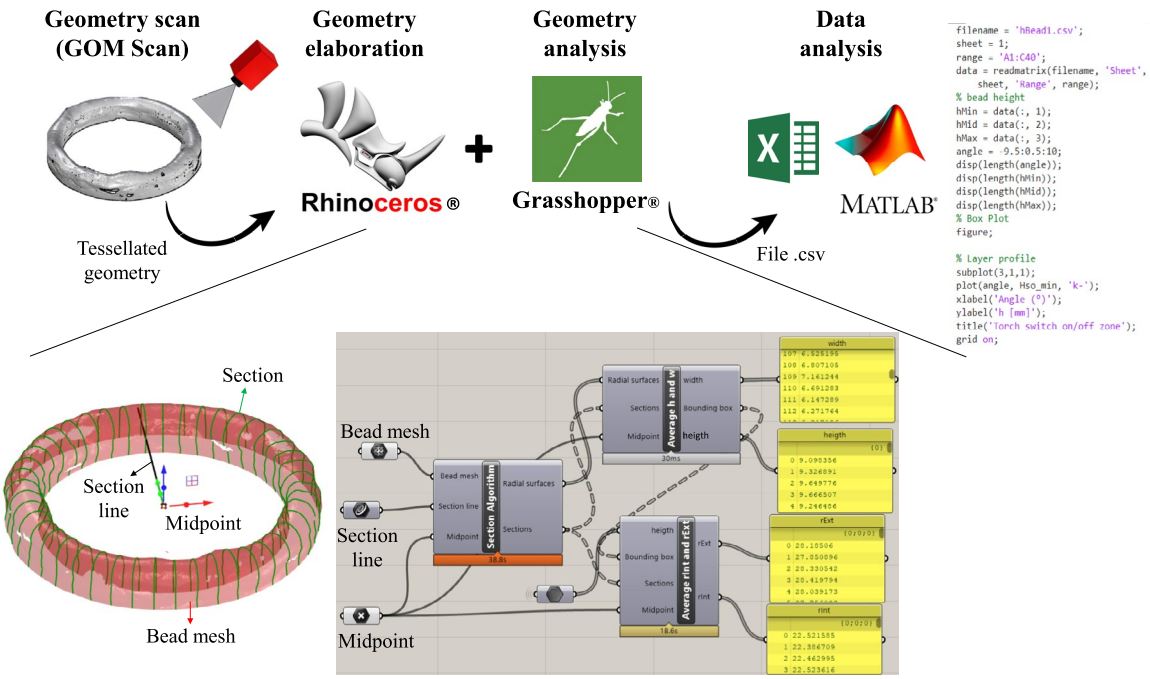

Fig. 4 Pipeline of the software tools to analyze the scans

Table 2 Specifications of the experimental setup

3D Printers	DELTA WASP 40×70 INDUSTRIAL
Material	Steel ISO 14341-A/G3Si1. Composition: C = 0.09%; Si = 0.82%; Mn = 1.41%; P = 0.011%; S = 0.005%; Cu = 0.023%; Ni = 0.019%; Mo = 0.006%; Cr = 0.25%
Shielding gas	Ar 85% + CO_2 15% (CORGON 15)
Gas flow rate	15 l/min
Welding generator	Fronius TPS 320i
Process type	CMT Continuous
Wire diameter	1.2 mm
Stick out	10 mm
Arc length	0
Impulse correction	0
Start/stop parameters	Default (defined by Fronius)

controller has been upgraded to communicate with the TPS 320i welding generator. The setup is controlled via G-code, which contains instructions for the printer motion system and the desired *WFR* value.

Figure 6 illustrates an example of the G-code. Specifically, it consists of three main parts, i.e., the start, the main, and the final sections. In the main section, the coordinates that describe the layer trajectories are defined, including the type of motion and speed. The *G5 S0* and *G5 S1* commands are specific for turning the torch off and on, respectively. Finally, pause times between layers can be specified.

The position of the last path target where the torch is switched off is analyzed as an input factor, in addition to *WFR* and *TS*. *TSOO* parameter allows the trajectory to be overlapped with the initially deposited material to avoid failures as the discontinuities in the deposition are highlighted in Fig. 2. In the executed experiments, *TSOO* was varied among *0*, *1*, and *2 mm* (Fig. 7). Trajectories have been discretized in small linear traits, whose length is limited to a minimum value of *3 mm* to avoid excessive discontinuities in the path.

Table 3 summarizes the implemented DOE. Three levels for each factor have been considered. Hence, the total number of specimens was 27, considering the full factorial approach with three levels and three factors.

Furthermore, the sequence of the trials was randomized with a specific function of MATLAB®, resulting in the working plan shown in Table 4. The randomization was

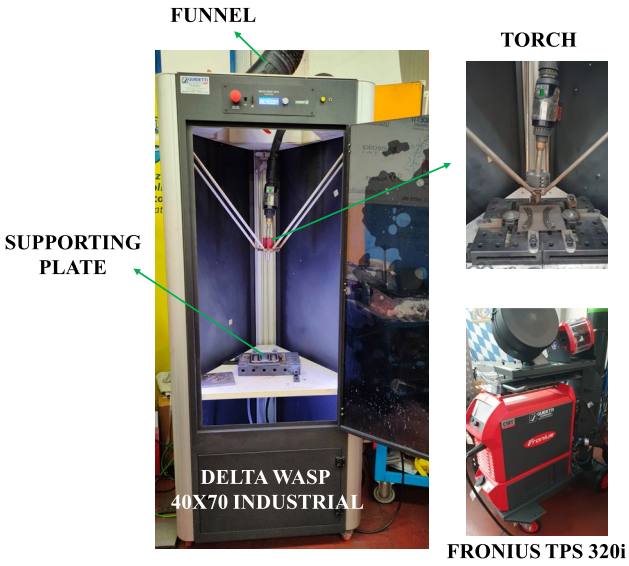

Fig. 5 Experimental setup

introduced to mitigate the effect of disturbance variables, such as geometrical inaccuracies, room temperatures, and substrate flatness.

Then, the specimens, whose nominal geometry is reported in Fig. 8, were produced using the described setup. A 3-min pause was added between each sample to restore the initial thermal conditions of the base plate. Additionally, a 45° rotation was applied to the path starting point on each layer curve, with these positions moved along the circumference to prevent the accumulation of defects that could occur if the starting point remained in the same location on the specimen. It is important to note that *TSOO* was applied to each layer.

Figure 9 shows two specimens, i.e., samples of substrate 5 and substrate 7 (refer to Table 4). It can be appreciated how the shape of the deposited material deviates from the nominal uniform one.

2.2 Scanning of the specimens

Each specimen was scanned using a GOM ATOS Core 200 structured light scanner (Fig. 10). This scanner uses a system consisting of an LCD projector that emits a light

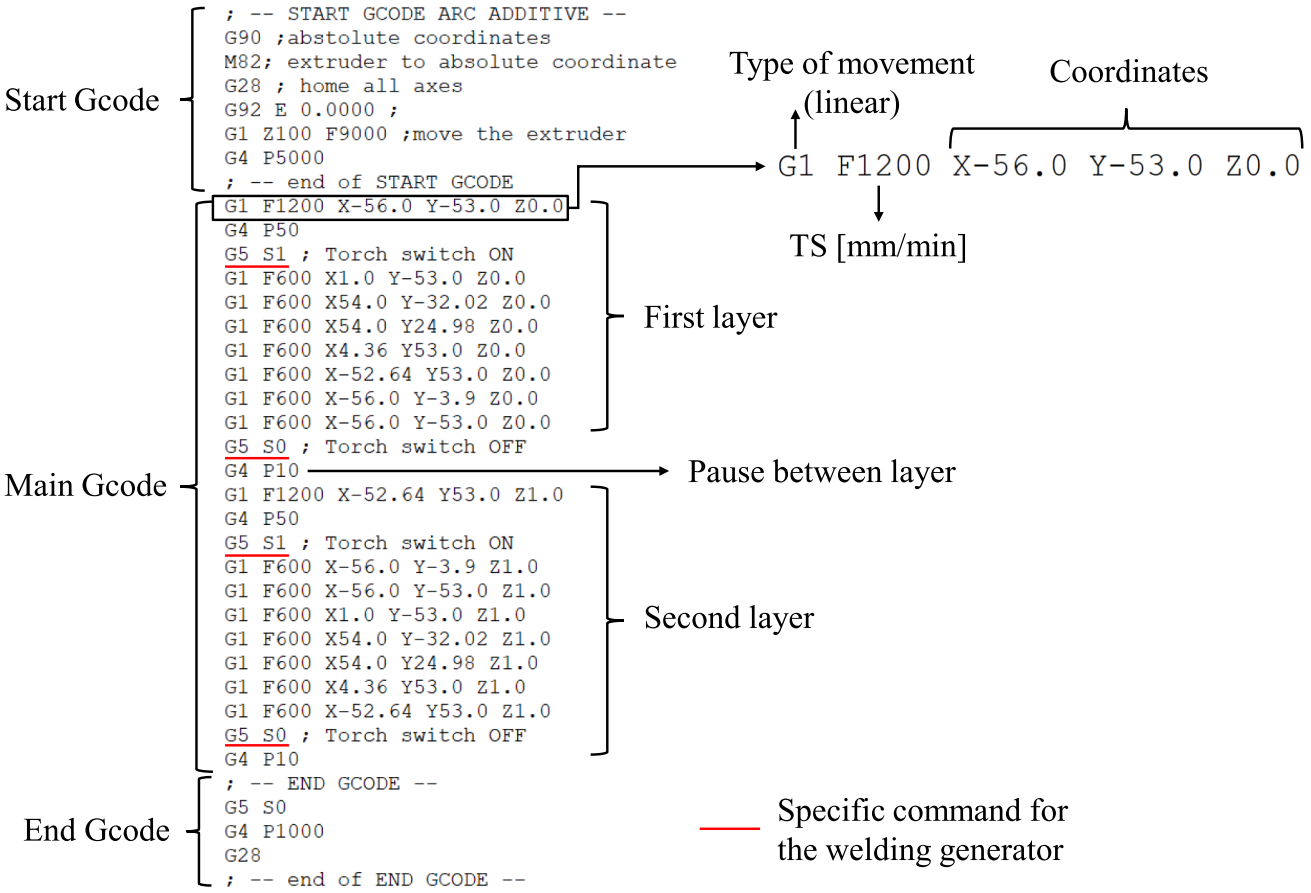

Fig. 6 Structure of the G-code program to control the DELTA WASP printer

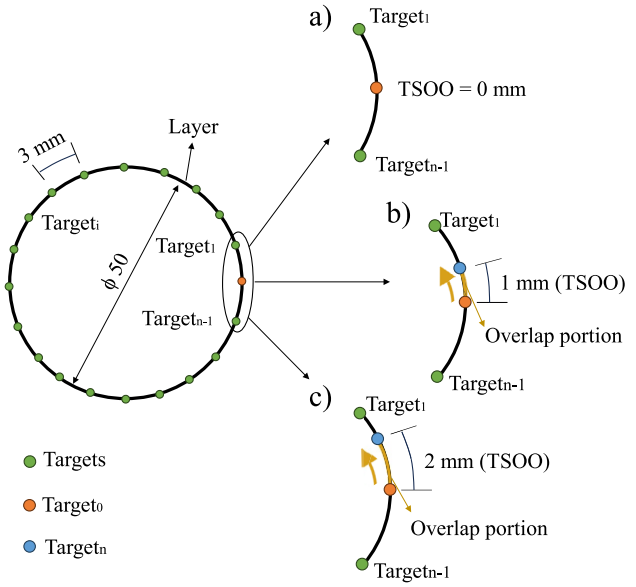

Fig. 7 Discretization of the deposition path

Table 3 Geometrical and technological parameters assumed in the experimental phase

Parameters	Values
TSOO [mm]	0, 1, 2
WFR [m/min]	1.5, 2, 2.5
TS [mm/s]	3, 4, 5
Layer height [mm]	1.2
Number of layers	5
Type of deposition	Layer by layer
Substrate [mm × mm × mm]	150 × 150 × 8
Sample diameter [mm]	50
CD *x* [mm]	65
CD *y* [mm]	65
Number of experiments	1
Number of samples (i.e., repetitions)	1
Total samples (each combination of parameters)	1

pattern on the part to be scanned. The pattern consists of fringes of blue light that minimize the interference due to other light sources and the effects of reflections compared to white light. The deviations of the realized specimens from the nominal conditions are at least one order of magnitude bigger than the scanner accuracy, confirming the validity and consistency of the presented approach.

The scanner is held vertically by a supporting frame above a rotating table, which can also be tilted thanks to a spherical joint. The part to be inspected can be secured on the table with screws and positioned in the needed orientation.

Table 4 Randomized plan of the executed experiments

No. of substrate	No. of sample	WFR [m/min]	TS [mm/s]	TSOO [mm]
1	1	2	3	1
	2	2	4	0
	3	2.5	3	0
	4	2.5	3	1
2	5	2.5	5	2
	6	1.5	3	2
	7	2.5	4	2
	8	2	5	2
3	9	2	3	2
	10	1.5	4	1
	11	2	4	2
	12	1.5	3	0
4	13	2	4	1
	14	1.5	5	1
	15	1.5	5	0
	16	1.5	5	2
5	17	2.5	5	1
	18	1.5	3	1
	19	2.5	5	0
	20	1.5	4	0
6	21	2	3	0
	22	2	5	0
	23	2	5	1
	24	2.5	4	0
7	25	2.5	4	1
	26	2.5	3	2
	27	1.5	4	2

Having relatively dark samples with some oxidized areas can reduce the acquisition quality, and the reflective behavior of the metal causes spots of missing data, also known as *holes*. Furthermore, acquiring the specimen from a limited number of viewpoints would lead to a partial reconstruction of the geometry because some portions might be obscured in the selected configurations. Therefore, the scanning procedure was codified in a predetermined sequence of repeatable positions to be obtained by rotating the table to get almost full surface coverage and comparable measuring conditions from plate to plate. In the proposed cases, the *holes* results in being sporadic and sometimes absent.

An initial acquisition is taken from a condition where the base is tilted *45°* from the vertical direction. Next, the base is rotated three times by *90°*. For each rotation, a new acquisition is made. After, a new orientation of the spherical joint between the base and the supporting frame is given to the table, which is orthogonal to the previous one. The new tilted position varies three times, thus having four total

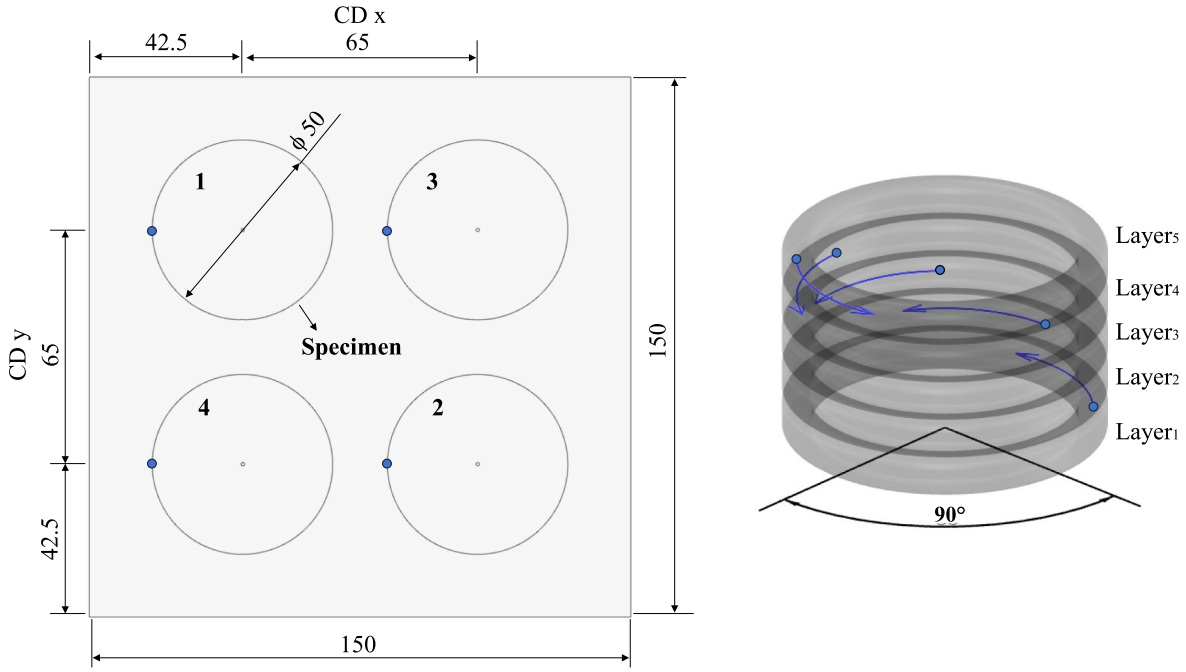

Fig. 8 Specimens manufactured from number 1 to 4. The blue dots in the right figure represent the starting points of each layer

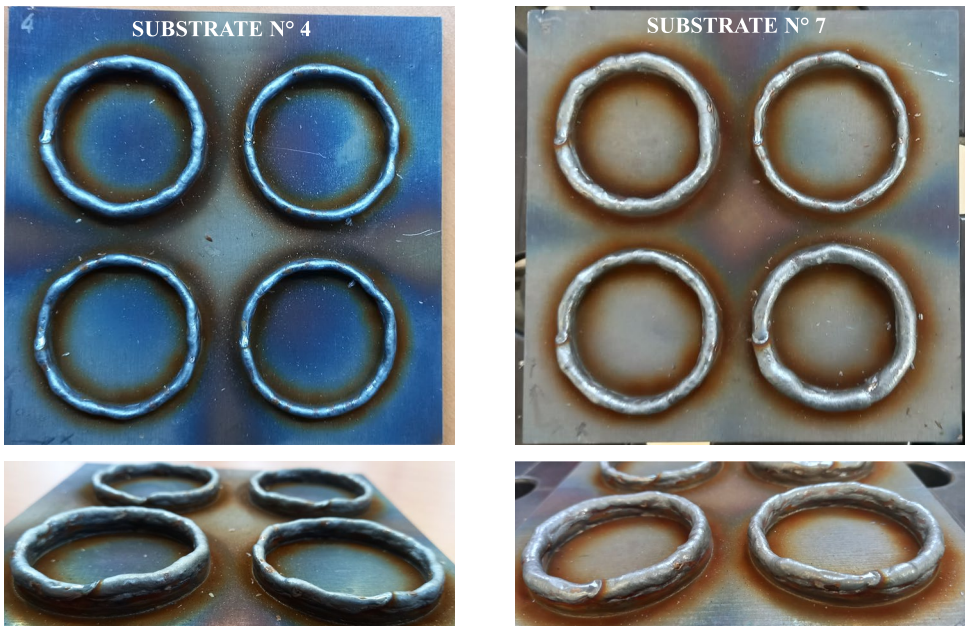

Fig. 9 Obtained specimens on substrate numbered with 4 and 7

configurations (Fig. 11). Therefore, the total number of acquisitions is 16.

Circular reflective markers randomly positioned on the plate surface (about 20 markers for each sample) have been used to align the different scans automatically, thanks to the native functionality of the scanner software (GOM Scan). A dense tessellated mesh is then obtained by merging each single scan and imported into the CAD environment in STL format. Each final mesh resulting from merging the 16 raw scans is made of about 2 million vertices and 3.5 million facets. The average distance between vertices was approximately *0.2 mm*.

Unlike 2D profiles obtained with laser sensors, this procedure enables a complete scan of the specimens, allowing an extended coverage of the shape which can be used for an in-depth analysis of the geometry in a CAD environment.

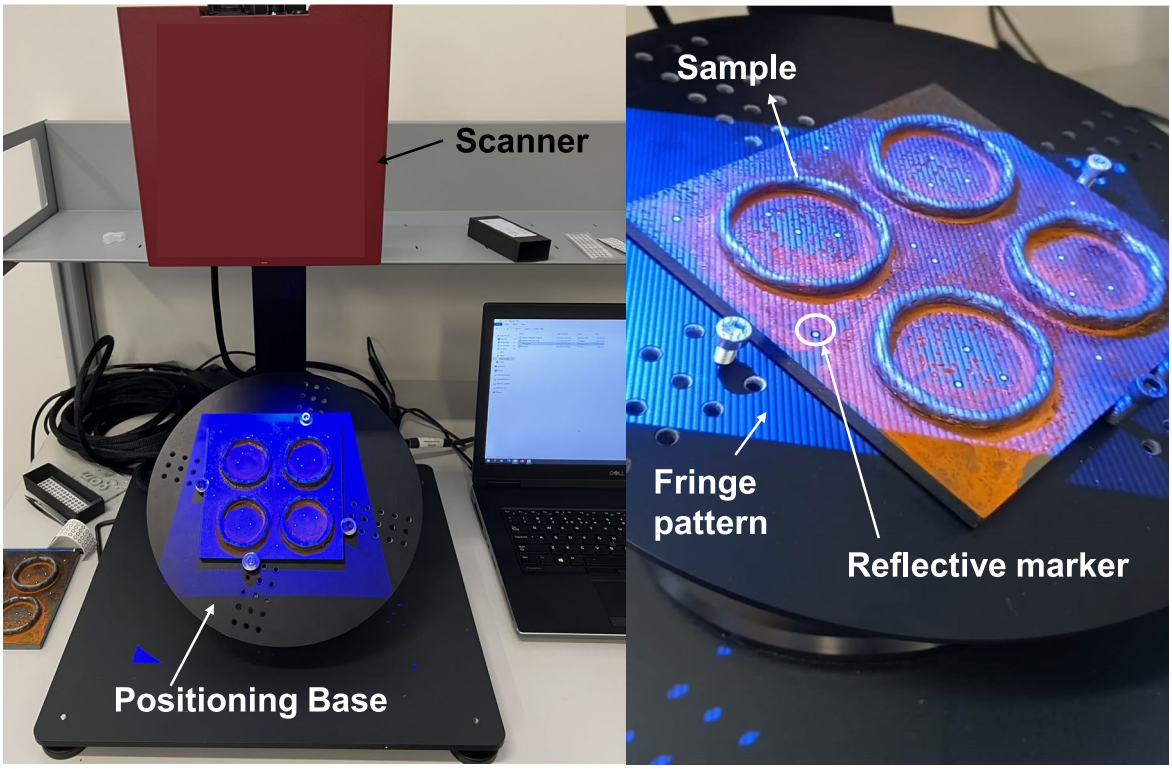

Fig. 10 GOM ATOS 200 3D blue-light optical scanner in its measurement setup

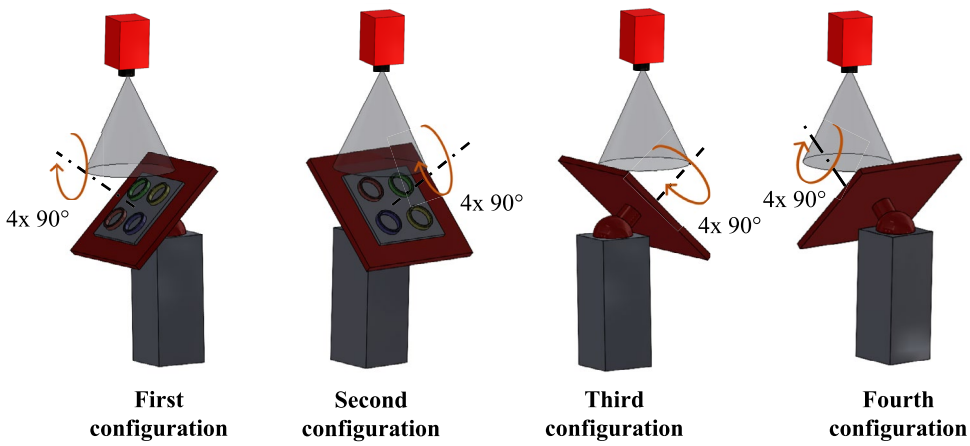

Fig. 11 Sequence of the 16 poses to maximize the scanning coverage

2.3 Geometry elaboration

The Rhinoceros® CAD software was used for the functionalities offered for the subsequent scanned geometry processing (Fig. 12). Initially, geometry is prepared for the analysis. Perimetral sections are extracted from the portion of mesh corresponding to the upper face of the substrate. A plane π is interpolated through the points of the sections using the native function of Rhinoceros®. Then, the mesh is rotated to align the obtained plane with the absolute reference system. A trimming plane π_t is created as an offset of the global XY plane at an elevation of $Z = 0.5\ mm$. The mesh is trimmed with π_t to remove the substrate that is not useful for the geometric analysis of the bead. The choice of an offset is motivated by the need to guarantee that the entire substrate is eliminated, also in consideration of the fact that the surface takes on a concave shape with raised edges due to the thermal distortion induced by the deposition of the material (as visible in Fig. 12). The lower portion of the bead that has been lost has been considered in the following by adding 0.5 mm to the heights of the beads being measured.

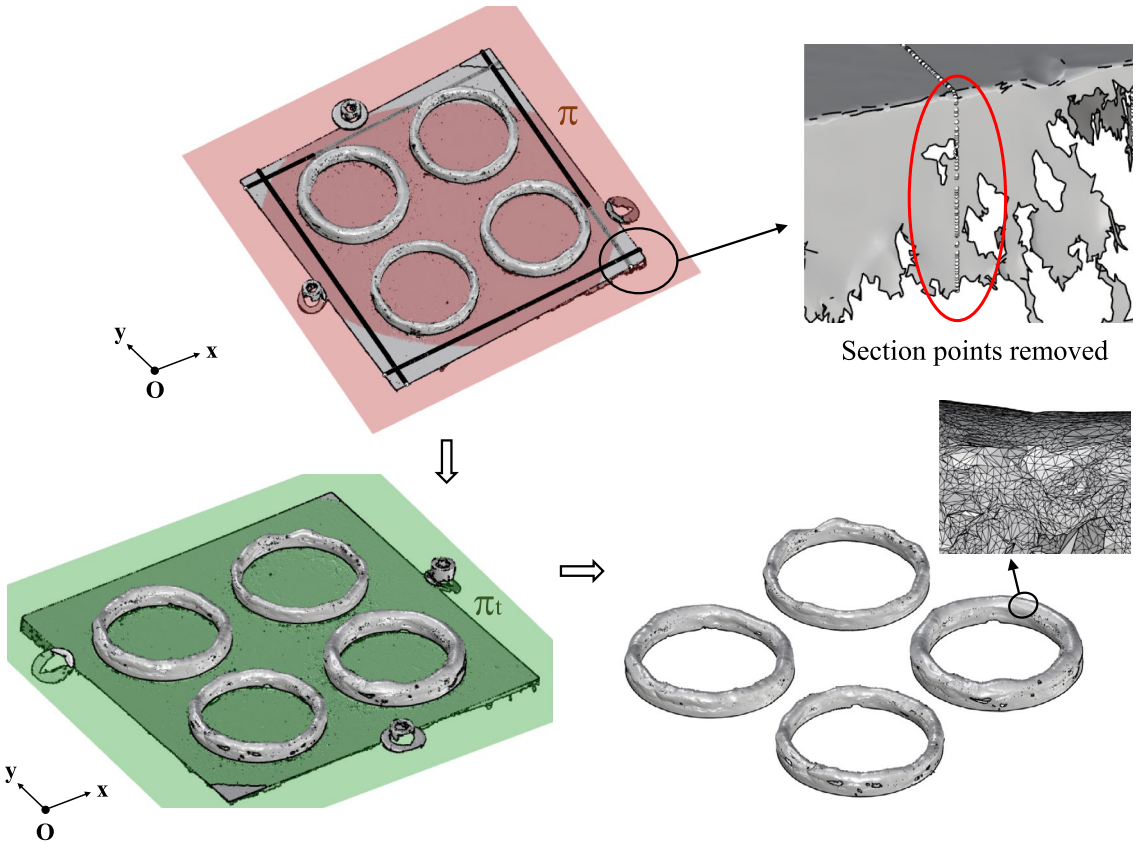

Fig. 12 Specimen orientation in the CAD environment and trimming of the substrate

The shape analysis is based on a series of radial sections. For this reason, it is necessary to identify the center of each specimen as the passing point of the common line of the sheaf of planes to intersect with the model. The first step is to calculate the bounding box of the bead and calculate the maximum height of the geometry. Then, the bead mesh is intersected with a plane at a given height (*40%* of the sample maximum height), thus obtaining reference polylines representing the inner and outer profile of the two sides of the mesh.

Then, the vertices of the intersection polylines are extracted (Fig. 13). These points are divided into two groups corresponding to the inner points set and the outer points set by thresholding the distance from the specimen center according to the nominal circle diameter. After, two circles are interpolated through the points. Finally, the midpoint of the two centers of the inner and outer circles is chosen as the center for the radial sections.

2.4 Analysis of bead geometry

Three indices from the scans are considered and automated using Grasshopper®:

- *Average bead height (h) and width (w)*. *h* and *w* are defined as the mean values of the height and the width of the bounding box of the radial sections along the bead.
- *Lateral bead waviness*. It is calculated as the standard deviation σ of the internal (*rInt*) and external (*rExt*) radii of each section at a given height until reaching 60% of the maximum bead height.
- *The distribution of bead heights in the zone where the torch is switched off*. The layer height profile is analyzed for each specimen in a region that spans from $-20°$ and $+20°$ according to the starting point of the deposition of the last layer.

To do so, a set of 360 radial sections S_i is created for each specimen at each degree of angle according to the center determined with the previous procedure. A bounding box aligned with the section plane is calculated for each section S_i. Then, the *h* and *w* for each section are given by the sizes of the bounding box as depicted in Fig. 14, correcting with the 0.5 mm offset at the base.

Initially, the influence of the *WFR* and *TS* parameters was studied, excluding the *TSOO*. In fact, the effect of the *TSOO* parameter is limited to the torch switch on/off area, which

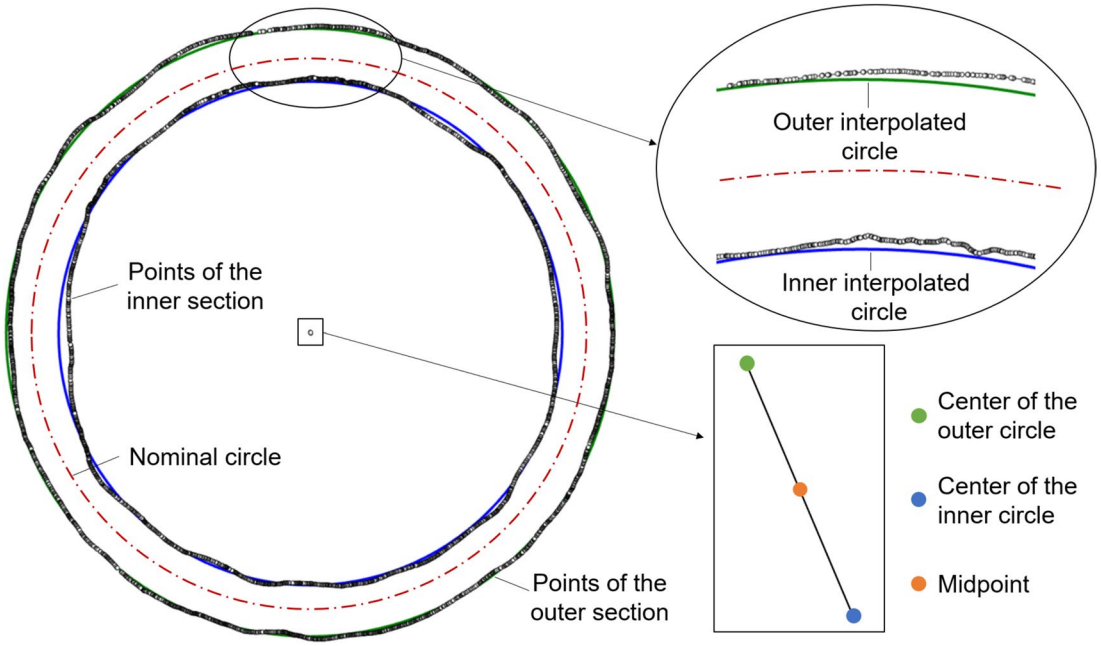

Fig. 13 Identification of the center of the sample by interpolation of an inner and outer circles at a reference height

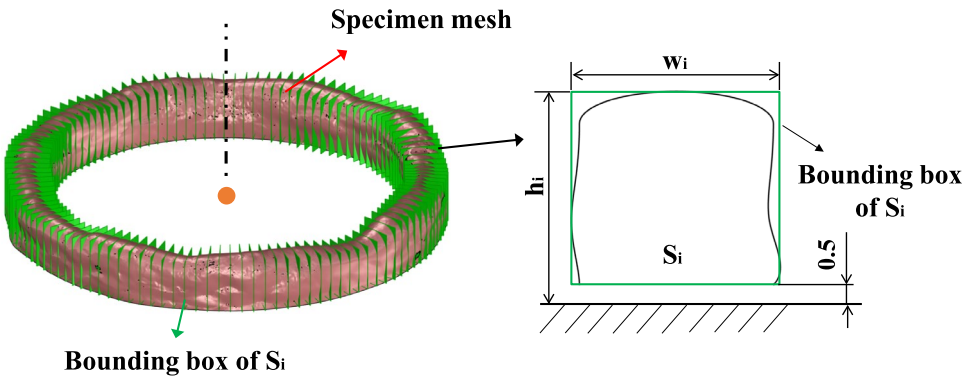

Fig. 14 Bead dimensions analysis. S_i: ith section; h_i: height of S_i; w_i: width of S_i

is analyzed separately. So, three samples are obtained for each parameter combination that differs in the *TSOO* values.

However, the average bead w value alone does not provide information on the lateral waviness of the sample. In this study, a characterization of undulations is provided by analyzing the 360 sections previously developed. Starting from π_t, a series of horizontal equidistant planes are created until they reach 60% of the maximum height of the sample. This value was set to exclude the curvature of the final bead portion. Two points are obtained for each plane intersected with one section, corresponding to the outer and inner profile respectively, as shown in Fig. 15a. The algorithm has been designed not to be affected by the presence of residual *holes* in the scan. In fact, the set of intersections may be empty, or only one point could be found. In the first case, the section is skipped, while in the second case the contribution of the point is still retained for the correct side.

Then, the distance between each intersection points and the center (orange point in Fig. 13) is calculated. The horizontal component of the distances is retained as the inner and outer radius of the specimen, $rInt_{ij}$ and $rExt_{ij}$ of S_i, as shown in Fig. 15b.

The last object of investigation concerns the torch switch on/off region of the last layer, in particular the influence of *TSOO* along with *WFR* and *TS*. The bead height is analyzed in a region that spans from $-20°$ and $+20°$ according to the starting point of the deposition of the last layer (Fig. 8). A total of 80 bead sections are then considered from this region, and the relative bounding boxes are used to calculate the bead heights (Fig. 14).

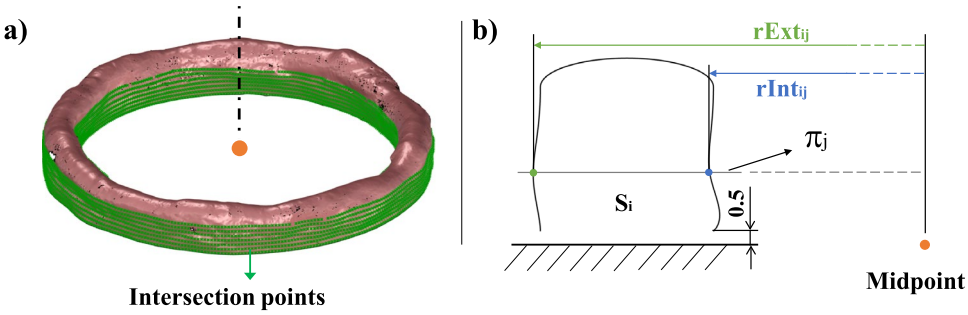

Fig. 15 Lateral waviness analysis

2.5 Statistical analysis of the measurements

Initially, an ANOVA analysis was conducted to determine to what extent the geometric parameters are influenced by the factors considered. Therefore, the average values of the height (h_{av}), the width (w_{av}), and the average height of the single layer (h_{s_av}) are calculated according to Eqs. 1, 2, and 4. The standard deviation of h (σ_h) and w (σ_w) are calculated according to Eq. 3.

$$h_{av} = \frac{\sum_{i=1}^{N} h_i}{N} \tag{1}$$

$$w_{av} = \frac{\sum_{i=1}^{N} w_i}{N} \tag{2}$$

$$\sigma_{h,w} = \sqrt{\frac{\sum_{i=1}^{N} (x_i - x_{av})^2}{N}} \tag{3}$$

$$h_{s\_av} = \frac{h_{av}}{f} \tag{4}$$

where h_i is the ith measured height, w_i is the ith measured width, x is one of the two analyzed parameters, N is the number of measures, and f is the number of layers, i.e., *5*.

Then, inner $rInt_{av}$ and outer $rExt_{av}$ average radii are calculated according to Eqs. 5 and 6, along with the relative standard deviations σ_{rInt} and σ_{rExt} (Eq. 7) that provide the measure of the surface waviness. In fact, high values of the standard deviation represent a high surface waviness. Equation 8 is used to calculate the mean circle radius (Fig. 13).

$$rInt_{av} = \frac{\sum_{i=1}^{N} rInt_i}{N} \tag{5}$$

$$rExt_{av} = \frac{\sum_{i=1}^{N} rExt_i}{N} \tag{6}$$

$$\sigma_{rInt,rExt} = \sqrt{\frac{\sum_{i=1}^{N} (x_i - x_{av})^2}{N}} \tag{7}$$

$$rMean_j = \frac{rExt_{av\_j} + rInt_{av\_j}}{2} \tag{8}$$

where $rInt_i$ and $rExt_i$ are the ith measured inner and outer radius, respectively, x is one of the two analyzed parameters, and N is the number of measures. The parameter $rMean_j$ is related to the jth mean circle radius of a specific combination of parameters, while $rExt_{av\_j}$ and $rInt_{av\_j}$ are the jth radii calculated according to Eqs. 5 and 6.

After, the two-way analysis of variance (ANOVA) with replication [46] has been used for the analysis of the data relative to the bead dimensions. This statistical method highlights the influence of two separate input factors, i.e., *WFR* and *TS*, on an output parameter, respectively h and w. Furthermore, the two-way ANOVA offers insights into the primary effect of each factor and the interaction between them.

The following three null hypotheses (H_0) have been verified:

(1) H_0: Mean level of the considered output is the same for all three *WFR* levels.
(2) H_0: Mean level of the considered output is the same for all three *TS* levels.
(3) H_0: No interaction between *WFR* and *TS*.

In case the three H_0 are rejected, it is possible to conclude that *WFR* and *TS* have a significant effect on the analyzed output and that there is interaction between the two parameters. Two methods can be employed to reject the null hypotheses. The *F*-test involves an assessment of the *F* ratio which needs to be above a critical level. Similarly, the null hypothesis is rejected if the *P*-value is below a certain level, usually assumed in *0.05*. Also, the plots of the main effects are presented [47] to compare the relative strength of the effects of the two factors, i.e., *WFR* and *TS*, on h and w.

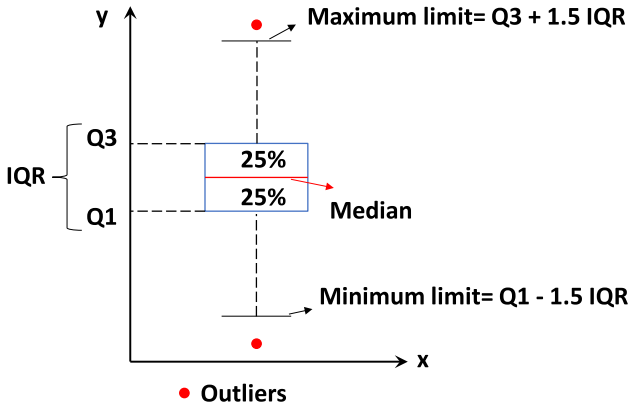

Fig. 16 Box plot data representation. Q1: first quartile; Q3: third quartile; IQR: interquartile range

3 Results from measured specimens

The boxplot graph (Fig. 16) is adopted to display data related to the first two analyses. Once the gather values are sorted, quartiles subdivide the values in equal portions each representing 25% of the samples. The median is the value containing the first half of the samples. Data between the first (Q1) and third (Q3) quartile limits are called the interquartile range (IQR). Additionally, minimum and maximum limits are defined as illustrated in Fig. 16, leading to the identification of outliers marked with red dots. In the plots reported in the next section, minimum and maximum limits are represented by respectively the minimum and maximum of the distribution, if the specific threshold of the outliers is not exceeded.

ANOVA is then applied to determine the dependency of the investigated outputs from the input parameters and the interaction between them using the functionalities provided by MS Excel®.

3.1 Statistical analysis of bead dimensions

Table 5 summarizes the average sizes of the beads. An initial outcome of the proposed method concerns the assessment of the bead dimensions, as it provides statistical values regarding the sizes of the thin-walled structure resulting from the deposition process and the deformations induced by multiple layers on top of each other. Three samples were available for each combination of parameters, given the three values of the *TSOO*. Since 360 measures were taken for each specimen, a total of 1080 measures were obtained for each combination of *WFR* and *TS*.

As expected, it can be noticed that h_{av} and w_{av} tend to increase with high *WFR* values and low *TS* values. This behavior confirms the results previously reported [28], but with different values due to the used shielding gas containing a higher percentage of CO_2. This causes a hotter welding pool and an increased material penetration (lower h_{av}). The correlation is less evident in w_{av} with the combination $\{WFR = 1.5\ m/min;\ TS = 4\ mm/s\}$ and when $WFR = 2\ m/min$ was used.

Figure 17 represents the nine box plots related to the *w* data analysis. These graphs provide additional information less evident from Table 5. In fact, higher maximum thickness limits are obtained with $TS = 3\ mm/s$ when $WFR = 1.5$ and $2.5\ m/min$. Again, the general trend is not respected with $WFR = 2\ m/min$.

However, as can be noted from Table 6, the *F* values of *WFR*, *TS*, and their relative interaction are higher than the critical values. Also, the *P*-values are less than the critical limit of *0.05*, allowing the three null hypotheses defined in Sect. 3.4 to be rejected. Therefore, it is possible to conclude that both input variables still influence the average thickness of the specimen despite the deviations recorded.

Figure 18 depicts the main effects of *w* related to the parameters *WFR* and *TS*. *WFR* has a stronger influence on *w* compared to *TS*. Note that *w* tends to increase with high values of *WFR* and low values of *TS*. However, *w* slightly increases with the value of $TS = 5\ mm/s$.

Figure 19 depicts the box plots of the *h* data. The behavior results to be comparable to *w* analysis, but here height variation is limited.

Table 7 and Fig. 20 depict the two-way ANOVA analysis and the main effects plot. The results overlap the behavior

Table 5 Average bead dimensions obtained varying *WFR* and *TS*

WFR [m/min]	TS [mm/s]	w_{av} [mm]	σ_w [mm]	h_{av} [mm]	σ_h [mm]	h_{s_av} [mm]
1.5	3	4.78	0.64	7.84	0.67	1.57
	4	4.81	0.48	7.43	0.52	1.49
	5	4.17	0.53	7.25	0.73	1.45
2	3	4.72	0.33	7.62	0.60	1.52
	4	4.98	0.83	8.19	0.98	1.64
	5	5.92	0.48	7.95	0.65	1.59
2.5	3	6.65	0.72	8.30	0.46	1.66
	4	5.34	1.07	7.65	1.18	1.53
	5	5.20	0.39	7.69	0.6	1.54

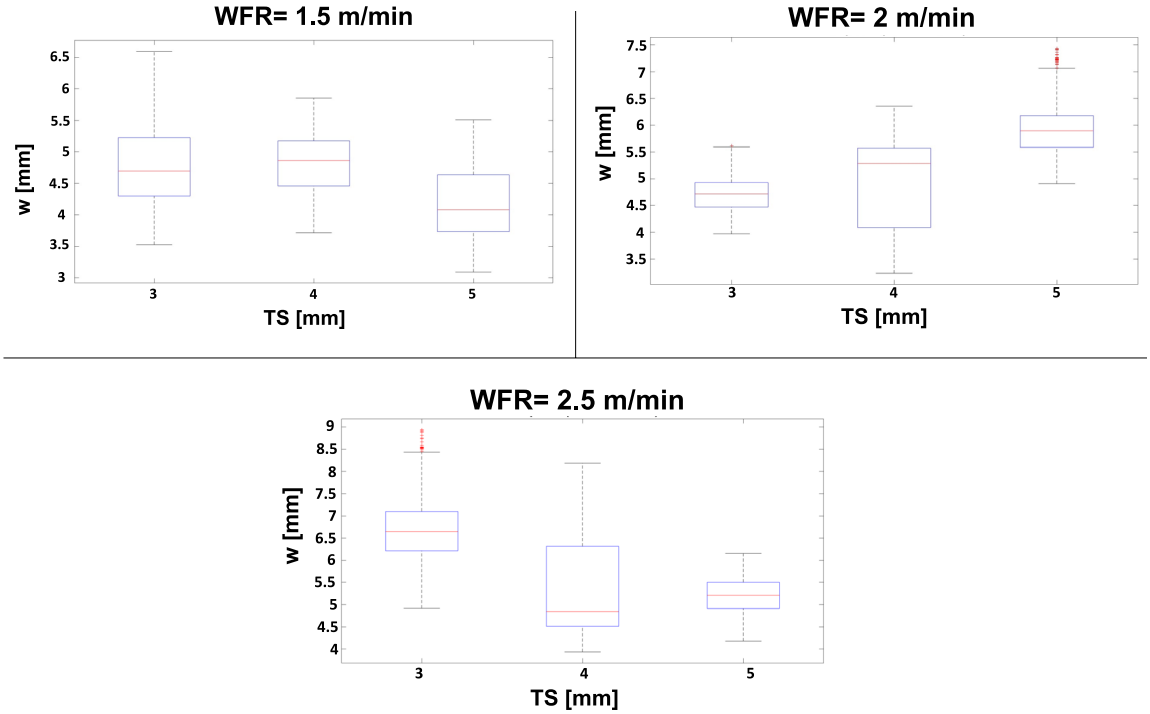

Fig. 17 Obtained results for the bead width (*w*)

Table 6 Results of the two-way ANOVA applied to the *w* dimension

Source of variation	Sum of squares	DoFs	Mean squares	*F*	*F* critic	*P*-value
WFR [m/min]	2121.46	2	1060.73	2540.10	3.00	0.00
TS [mm/s]	215.74	2	107.87	258.31	3.00	0.00
Interaction	2309.44	4	577.36	1382.58	2.37	0.00
Error	4055.27	9711	0.42			
Total	8701.91	9719				

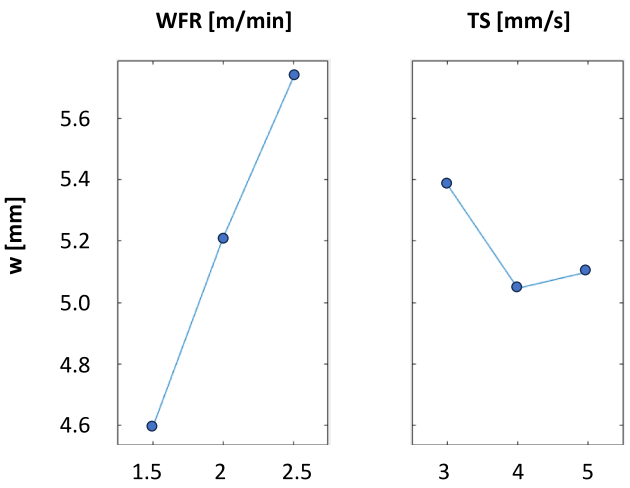

Fig. 18 Plots of the main effects of *w*

of *w* dimension. In this case, the *h* tends to slightly decrease with *WFR* = *2.5 m/min*, showing an opposite trend compared to the expected one (Fig. 20).

The results confirm that the bead dimensions can be controlled by varying the analyzed process parameters. Also, for the specific experimental setup, the primary effects hint to maintain the *TS* within a *3–4 mm/s* range while adjusting the *WFR* to modify the *w* dimension. Conversely, the *WFR* should be selected within a *1.5–2 m/min* range, with variations in the *TS* to control *h*. According to the gather data, these ranges ensure a good predictability of the bead dimensions.

3.2 Lateral bead waviness

Regarding the bead surface waviness analysis, *WFR* and *TS* are also analyzed as varied parameters. Again, three samples were available for each combination of parameters, given the tests available with three different *TSOO* values. Initially,

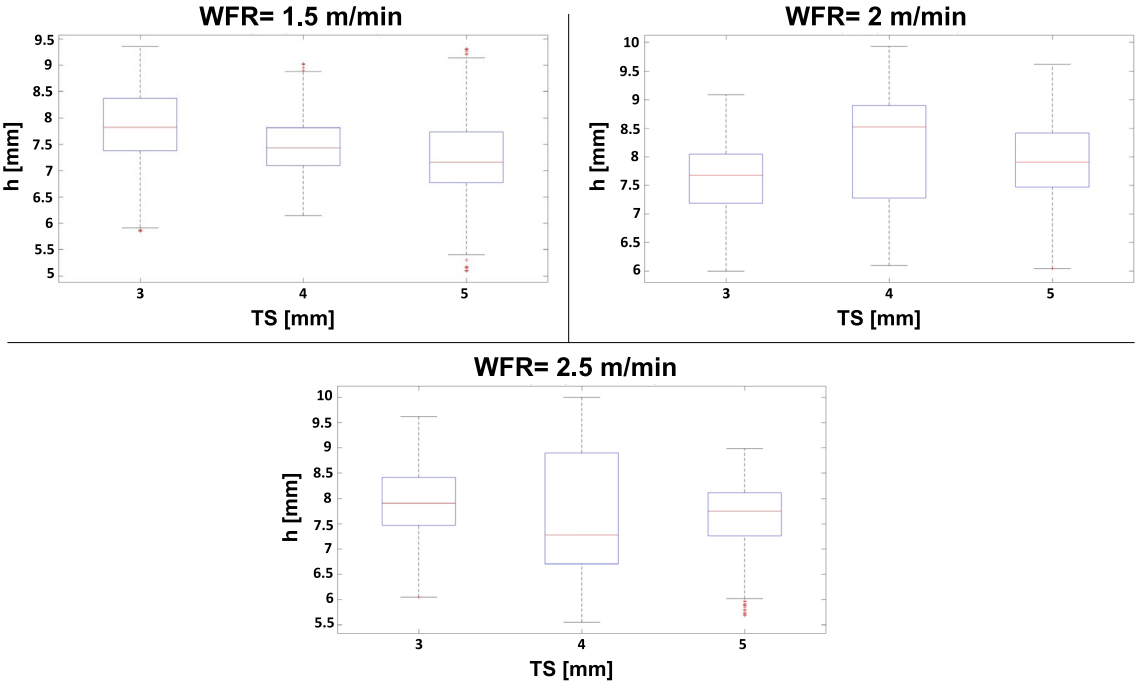

Fig. 19 Obtained results for the bead height (*h*)

Table 7 Results of the two-way ANOVA applied to the *h* dimension

Source of variation	Sum of squares	DoFs	Mean squares	*F*	*F* critic	*P*-value
WFR [m/min]	336.82	2	168.41	306.31	3.00	0.00
TS [mm/s]	136.90	2	68.45	124.50	3.00	0.00
Interaction	524.62	4	131.16	238.55	2.37	0.00
Error	5339.22	9711	0.55			
Total	6337.57	9719				

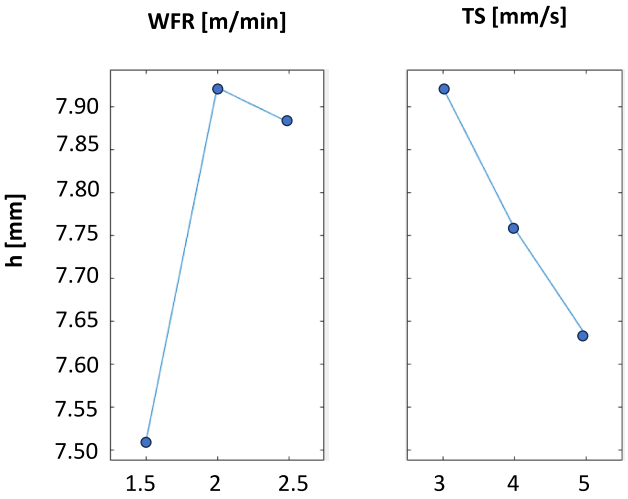

Fig. 20 Plots of the main effects of *h*

the two-way ANOVA analyses were repeated for both *rInt* and *rExt*, and the results confirm the dependence on *TS* and *WFR*. Details have not been reported here for brevity, since they do not provide any added value to the results for the *w* dimension reported in the previous sub section.

Waviness analyses are reported separately for the inner and outer surfaces. Table 8 summarizes $rInt_{av}$ and σ_{rInt} for each set of parameters, along with the registered range of *rInt* values.

As a first comment, *rInt* increases when low *WFR* and high *TS* values are set, because the bead becomes narrower. Again, this phenomenon seems to be opposite in the tests with *WFR = 2 m/min* (Fig. 21).

To provide an overall picture of the waviness variation, Fig. 22 reports σ_{rInt} depending on the process parameters. The minimum deviations are observed at *TS = 3 mm/s* and *WFR = 1.5–2 m/min*, leading to the best quality of the internal lateral surface.

Table 8 Lateral bead waviness: *rInt* analysis, considering only *WFR* and *TS*

WFR [m/min]	TS [mm/s]	$rInt_{av}$ [mm]	σ_{rInt} [mm]	$rInt_{max}$ [mm]	$rInt_{min}$ [mm]
1.5	3	23.12	0.29	24.09	22.25
	4	23.19	0.32	24.20	21.81
	5	23.34	0.37	24.35	22.15
2	3	23.07	0.28	23.92	22.15
	4	22.97	0.46	24.30	21.58
	5	22.54	0.38	23.53	20.72
2.5	3	22.14	0.56	23.33	19.72
	4	22.72	0.64	23.95	20.51
	5	22.84	0.32	23.90	21.78

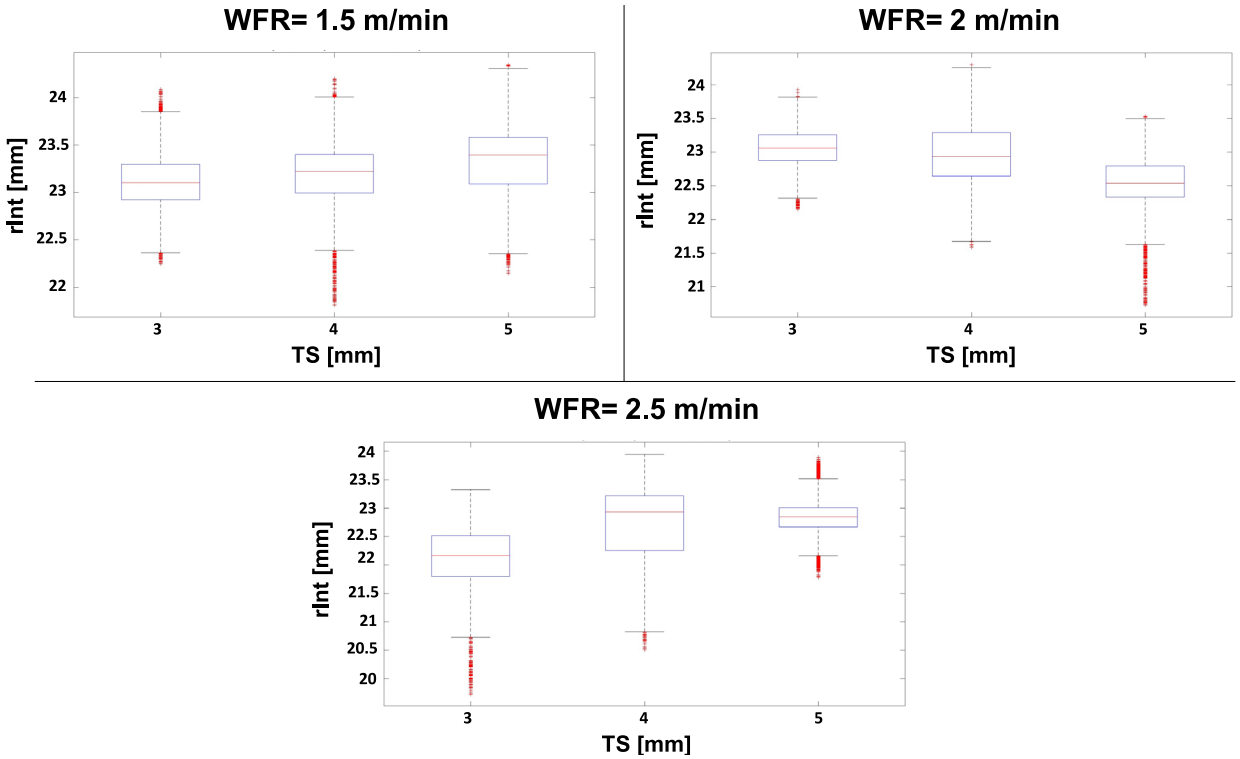

Fig. 21 Obtained results for the bead inner radius (*rInt*)

Conversely, *rExt* presents the opposite behavior to *rInt*. In fact, the bead widens when high *WFR* values and low *TS* values are set (Table 9).

Figure 23 shows the results graphically. The box plots present a smaller number of outliers compared to *rInt* box plots. The lowest standard deviations are obtained using $WFR = 2$ *m/min* and $TS = 3$ mm/s for both *rInt* and *rExt*.

The trend of σ_{rExt} is depicted in Fig. 24. In this case, the lowest standard deviation is obtained with $TS = 3$ *mm/s* and $WFR = 2$ *m/min*. Overall, σ_{rExt} is lower than that the variation obtained for *rInt*, highlighting that the external surface turns to be less wavy.

Finally, the gathered data allows an additional observation to be drawn relative to the mean radius *rMean* of the deposited circular bead defined by Eq. 8. The results summarized in Table 10 show that *rMean* regularly exceeds the nominal value of *25 mm*.

3.3 Torch switch on/off zone analysis

Finally, the torch switch on/off zone analysis data are reported in Table 11. Equations 1 and 3 are used to calculate the average height of the beads (h_{av}) and the relative standard deviation (σ_h), while *Dh* represents the absolute variation of the height, i.e., $h_{Max} - h_{Min}$.

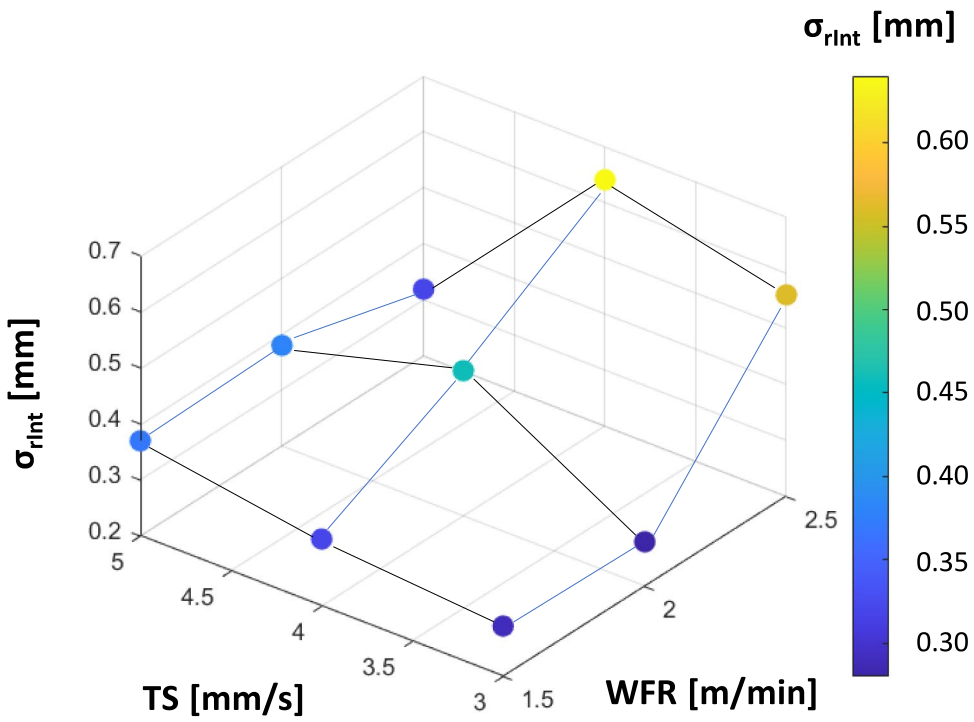

Fig. 22 Resulting values for σ_{rInt} depending on *WFR* and *TS*

Table 9 External bead waviness: *rExt* analysis, varying *WFR*, and *TS*

WFR [m/min]	TS [mm/s]	$rExt_{av}$ [mm]	σ_{rExt} [mm]	$rExt_{max}$ [mm]	$rExt_{min}$ [mm]
1.5	3	27.33	0.32	28.18	26.54
	4	27.22	0.29	28.28	23.19
	5	27.08	0.25	27.89	26.18
2	3	27.30	0.22	28.24	26.66
	4	27.44	0.38	28.43	26.31
	5	27.87	0.30	28.90	27.00
2.5	3	28.07	0.37	29.34	26.73
	4	27.61	0.47	29.20	26.39
	5	27.56	0.30	28.63	26.65

Figure 25 depicts the height profile of two specimens with opposite behavior. The angle position where the torch is switched off is highlighted, while the *0°* angle corresponds to the point where the torch has been switched on.

Sample 25 has the lowest σ_h, and the height profile according to the angle range is reported in the upper part of Fig. 25. On the contrary, specimen 17 has the highest standard deviation, indicating a more marked variation in height than the other specimens. This behavior is highlighted by the graph in the lower part of Fig. 25. As can be noted, the layer height varies up to *3.11 mm*.

Figure 26 in the Appendix collects the other height profiles of the entire set of samples. As a first consideration, neither of them presents the problem shown in Fig. 2. Furthermore, an interesting indication of the influence of *TSOO* seems to emerge. Looking at the data reworked in Table 12, the adoption of a TSSO equals to 2 mm produces a stabilization of the height of the beads, which can be observed both as reduction of the 17% of the absolute variation of the heights registered in the area, and similarly in the reduction of a 27% of the relative standard deviation.

3.4 Discussion and guidelines for the process planning of WAAM parts

The presented work ultimately provides guidelines for the design and process planning of components, focusing on the key phenomenological aspects for successful realization with WAAM technology.

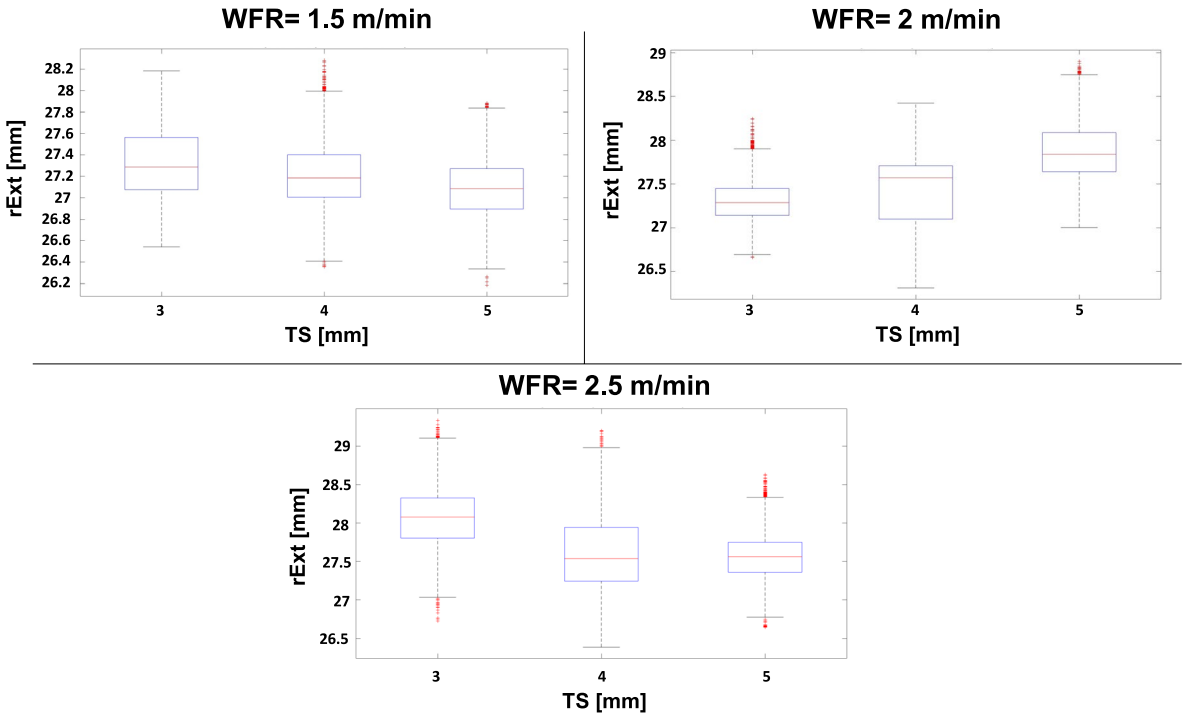

Fig. 23 Obtained results for the bead outer radius (*rExt*)

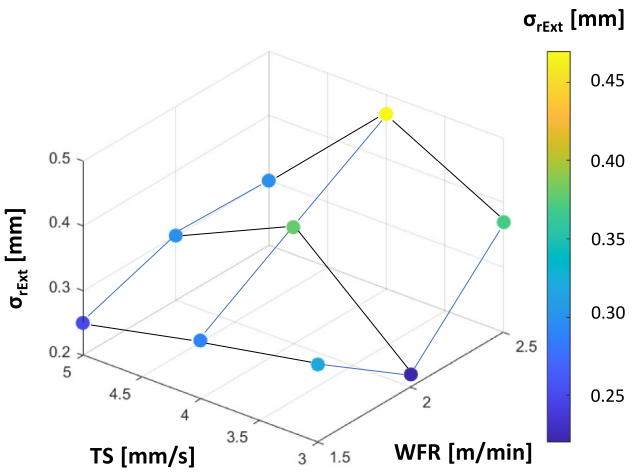

Fig. 24 Resulting values for σ_{rExt} depending on *WFR* and *TS*

Table 10 Computation of *rMean* depending on *WFR* and *TS*

WFR [m/min]	TS [mm/s]	$rExt_{av}$ [mm]	$rInt_{av}$ [mm]	rMean [mm]
1.5	3	27.33	23.12	25.23
	4	27.22	23.19	25.21
	5	27.08	23.34	25.21
2	3	27.30	23.07	25.19
	4	27.44	22.97	25.21
	5	27.87	22.54	25.21
2.5	3	28.07	22.14	25.11
	4	27.61	22.72	25.17
	5	27.56	22.84	25.20

A first significant finding is related to a certain instability registered in the relationships between the sizes of the beads and the working parameters, even though the expected correlations have been confirmed by the ANOVA as well as reported in the literature. Such deviations are connected to the adjustments made by the welding generator of the process, including provided heat power, according to characteristic curves implemented by the supplier. Even though such a mechanism was originally designed as a valuable means of control against variable welding conditions, the induced corrections in the power output affect the fine tuning which is required in WAAM applications. To a lesser extent, the deviations are attributable to inaccuracies in the control of the wire feed, i.e., *WFR*, and of the robot movement, i.e., the ability to maintain the imposed TS.

Therefore, the reported variabilities need to be considered in the design and realization phase of a certain part, for instance by depositing an optimal amount of

Table 11 Data obtained varying the *TSOO* parameter

No. sample	WFR [m/min]	TS [mm/s]	TSOO [mm]	h_{av} [mm]	h_{Max} [mm]	h_{Min} [mm]	Δ_h [mm]	σ_h [mm]
12	1.5	3	0	7.57	7.94	7.26	0.68	0.24
18			1	8.24	9.00	7.65	1.35	0.51
6			2	7.44	7.72	6.97	0.75	0.27
20		4	0	7.25	8.18	6.40	1.78	0.67
10			1	7.48	7.88	7.05	0.83	0.28
27			2	7.52	8.21	6.92	1.29	0.37
15		5	0	6.74	7.04	6.40	0.64	0.19
14			1	7.63	7.82	7.46	0.36	0.11
16			2	6.56	7.10	5.91	1.19	0.40
21	2	3	0	7.06	7.84	6.46	1.38	0.49
1			1	7.69	8.04	7.15	0.89	0.31
9			2	8.18	8.34	7.96	0.38	0.10
2		4	0	8.52	8.75	8.28	0.47	0.16
13			1	7.13	7.65	6.36	1.29	0.47
11			2	8.69	9.20	8.30	0.90	0.29
22		5	0	8.36	8.67	8.00	0.67	0.22
23			1	7.63	7.99	7.17	0.82	0.30
8			2	7.26	7.39	6.97	0.42	0.09
3	2.5	3	0	8.32	8.65	7.78	0.87	0.27
4			1	8.45	8.67	8.15	0.52	0.16
26			2	7.64	7.99	7.37	0.62	0.23
24		4	0	6.74	7.14	6.62	0.52	0.10
25			1	9.37	9.44	9.31	0.13	0.03
7			2	6.55	6.90	5.83	1.07	0.28
19		5	0	6.75	8.05	5.69	2.36	0.94
17			1	7.18	8.98	5.87	3.11	1.15
5			2	8.33	8.83	7.66	1.17	0.36

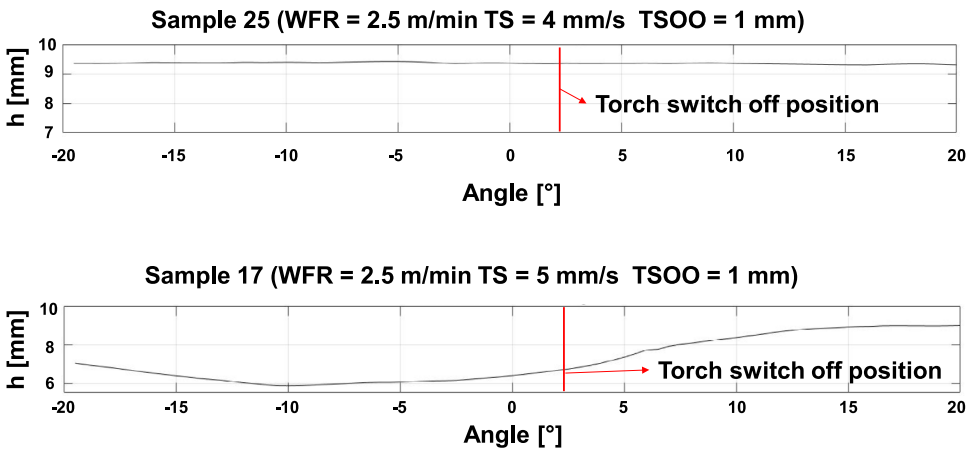

Fig. 25 Heights of sample 25 and 17 in the torch switch on/off zone

extra material for subsequent post-processing steps. Such behavior has been neglected in the works analyzed from the literature, apart from adopting closed loop systems to measure the deposited beam and adjusting the working parameters in real time. Setups have been reported based on profile measurement, in situ monitoring of welding power and online adaptation of welding parameters. This is certainly a valuable solution but may fail to provide timely corrections. Since the recorded variations can be attributed to the nature of the short-circuit process and the

Table 12 Influence of the *TSOO* parameter on the height variability in the torch switch on/off zone, i.e., the absolute height variation D_h and the relative standard deviation s_h

D_h [mm]	TS [mm/s] WFR [m/min]	TSOO = 0 [mm]			TSOO = 1 [mm]			TSOO = 2 [mm]		
		3	**4**	**5**	**3**	**4**	**5**	**3**	**4**	**5**
	1.5	0.68	1.78	0.64	1.35	0.83	0.36	0.75	1.29	1.19
	2	1.38	0.47	0.67	0.89	1.29	0.82	0.38	0.90	0.42
	2.5	0.87	0.52	2.36	0.52	0.13	3.11	0.62	1.07	1.17
	Average	**1.041**			**1.033 (− 1%)**			**0.866 (− 17%)**		
σ_h [mm]	**TS [mm/s] WFR [m/min]**	**TSOO = 0 [mm]**			**TSOO = 1 [mm]**			**TSOO = 2 [mm]**		
		3	**4**	**5**	**3**	**4**	**5**	**3**	**4**	**5**
	1.5	0.24	0.67	0.19	0.51	0.28	0.11	0.27	0.37	0.40
	2	0.49	0.16	0.22	0.31	0.47	0.30	0.10	0.29	0.09
	2.5	0.27	0.10	0.94	0.16	0.03	1.15	0.23	0.28	0.36
	Average	**0.364**			**0.369 (+ 1%)**			**0.266 (− 27%)**		

variability of heat input and heat dissipation, the need for the proposed process characterization to ensure accurate prediction of the final geometry is confirmed.

A second contribution of the proposed approach regards the measurement of the lateral surface quality of the specimen. In the literature, surface waviness concept is connected to the effective wall width after machining away all the surface irregularities [48] and determines the amount of material to be removed [49]. The measurement of surface waviness is fundamental for the prediction and optimization of the irregularities, as the work reported in [50] even if applied to the upper surface formed by multiple beads deposited side by side. From the elaborated experimental data, it is confirmed that it is preferable to use lower *WFR*, as it tends to a smoother and more uniform weld bead by minimizing the amplitude of surface irregularities [51]. This enhances the overall quality of the weld by ensuring a higher surface finish and dimensions stability, which has been demonstrated in this work in the specific case of multilayered thin walls made by CMT technology.

Another result emerges from the adopted circular shape of the specimens that cannot be observed on similar experiments made on straight beads reported in the literature [52]. The data reported in Table 10 show a deviation of the mean radius of the specimens compared to the nominal one, namely the tendency for the external radius to expand more than the internal radius in curved paths. This phenomenon holds significant relevance in the path planning of WAAM. The main cause could be related to an accumulation effect that pushes the material towards the outside or to an inaccuracy in the path followed by the robotic arm. This calls for the necessity of introducing corrections in the paths generated by slicing software to compensate for deviations. In more general cases, the shape of the workpiece can be further enhanced by FEM simulations to foresee and to compensate for errors, acting on deposition parameters and inner structures as demonstrated in the literature [53].

Finally, the behavior of the torch switch-on/off zone of closed layer paths has been examined. First of all, the variation of the starting point of deposition in closed paths at each layer is beneficial for a better regularity of the realized thin walls and to avoid major failures such as bead discontinuities (see Fig. 2). Furthermore, the introduction of *TSSO*, i.e., an overlapped trait between the initial and final portion of a closed bead, seems to help the regularization of the height on the junction zone, which has been observed with *TSSO* = *2 mm*. The absolute variation of the height and the relative standard deviation have significantly reduced. Since collected data are variable and quite discordant, additional experiments are advisable to confirm

the correlations between the height profile and the *TSOO* parameter.

4 Conclusions and future directions

This paper presented a method and the relative implementing procedure for an accurate geometrical assessment of specimens obtained by WAAM. Samples are scanned using a 3D structured light scanner to obtain digital geometry to be processed and analyzed in a CAD environment in a formalized manner. The approach exploits the capability offered by offline acquisitions by optical scanners to guarantee complete shape coverage and protects against dependence on the human factor.

The results of a preliminary data gathering campaign highlight that the procedure can be successfully employed for an accurate characterization of the bead dimension and shape according to the input parameters. First, the average height and width of samples were investigated according to varied process parameters (*WFR*, *TS*, and *TSOO*). Also, the two-way ANOVA analysis was performed, confirming the correlation of the analyzed parameters with the bead dimensions, which is fundamental for implementing non-uniform slicing and infill strategies. The second analysis focused on the characterization of the lateral surface waviness. In particular, the standard deviation value is used as an index of the surface quality and the expected geometrical accuracy of the part. Finally, the torch switch on/off area was studied to reduce the oscillations of the height profile by introducing an overlapping trait in the deposition path. The specimens have revealed a good statistical correlation between the analyzed parameters and the measured geometry, even though some shape and dimensional variabilities have been registered. This led to the formulation of some process design guidelines, as well as the suggestion to introduce measurement systems to acquire the actual amount of wire feed, the speed maintained by the welding torch, and the instantaneous electrical power generated by the welder during deposition.

In conclusion, the proposed approach is useful as a formal and repeatable procedure to objectify the influence of several process factors to search for optimal deposition conditions capable of the required precision in the final part. The variations in the bead dimensions need to be assessed and considered to avoid the presence of voids and missing portions in the realized artifact. Furthermore, if some portions of the part require machining as post-processing activities to achieve the prescribed dimensional and geometric tolerances, as well as the required roughness, the minimum amount of extra material can be correctly evaluated.

The experimental campaign needs to be expanded in the future, considering more parameters that influence the process. In addition to the settings of the welding generator, robot motion, material and gas types, and thermal effects must be considered. In fact, the obtained results are valid in comparable configurations where the material is deposited close to the substrate, given the limited number of stacked layers being considered and the strong dissipating action of the substrate. Further extension of the work also foresees the identification of correlations between measured waviness and irregularities and the structural integrity and performances of the manufactured part. The goal is the definition of a complete simulation of the deposition that expands the models present in the literature by including residual stresses, mechanical properties, and the prediction of the expected geometry of the deposited bead according to the results reported in this study, also supported by machine learning elaborations if collected data are sufficient.

Appendix

Table 13 Bead geometry characterization approaches from literature. This includes generator type, considered parameters, measured characteristics of the bead, material, and implemented shielding gas. Column *Model* reports whether a predictive model for the bead dimensions as a function of process parameters has been proposed. The adopted means of measurement are highlighted, as well as if the realized specimens were multi-layer (ML). A star marks a study made on multi-layered samples, although not focused on the bead geometry analysis

Work	CMT	Parameters	Output	Material	Gas	Model	Means of measures	ML
[19]	Yes	WFR, TS	h, w	Carbon steel	Ar 90%; CO_2 10%	Response surface	Caliper	Yes
[21]	No	WFR, TS, current, gas flow rate	h, w, wetting angle, p, roughness	HASTELLOY X	Ar	No	SEM	Yes
[25]	No	WFR, TS, torch angle, current	h, w, p, molten pool width	Mild steel	Ar 95%, CO_2 5%	Teaching–learning based optimization	Microscope	No
[29] (strut)	No	Current, WFR, voltage, arc discharge time, time interval, torch angle	h, w	YGW16	Ar 80%, $C0_2$ 20%	No	Computer tomography	No
[30, 54]	Yes	WFR, TS	h, w	Copper coated steel	\	Neural Network	3D Laser profile scanner	No
[31]	Yes	WFR, TS	h, w	ER70S-6	Ar 80%, CO_2 20%	Math models	2D profilometer	No
[33]	Yes	WFR, WFR/TS	h, w, p	Hot-rolled S355	Ar 80%, CO_2 20%	Linear regression	Stereo microscope	No*
[34]	Yes	WFR, current, voltage	h, w	6061-T6 aluminum	Ar	No	Camera	Yes
[37]	No	WFR, TS, interpass temperature	Hardness, total wall width, flatness deviation	G 42 4/M21 3Si1	Ar 85%, CO_2 15%	No	Camera	Yes
[54]	No	WFS	w	\	\	No	Monocular cameras	No
[55]	No	Peak current, WFR, TS	h, w	5A06 aluminum alloy	Ar	Regression model (ANOVA)	\	\
[56]	No	Voltage, WFR, TS	h, w	Copper-coated mild steel	Ar 82%, CO_2 18%	Neural Network	Coordinate measuring machine	No
[57]		WFR, TS	h, w	Steel	Ar	Response surface	Multifocal acquisition	No
[58]	No	Voltage, Current, TS	h, w, p	316L	Ar	Decision matrix	Mitutoyo caliper	No
[59]	No	WFR, TS, voltage	w	Al2325	Ar	Regression	Laser scanner	Yes
[60]	No	WFR, TS, voltage, current, cooling power	h, w	Al2325	Ar	No	Laser distance sensor	Yes
[61]	Yes	WFR, TS	h, w	ER70S-6	Ar 82%, CO_2 18%	No	Gauge USHS-4, Mitutoyo caliper	Yes
[62]	No	Peak current, WFR, TS	h, w	\	\	Multi-gene	\	No
[63]	No	WFR, TS, current, voltage	h, w	Low carbon steel	Ar 95%, CO_2 5%	Deep learning	Infrared camera, LATM sensor	No
[64]	Yes	WFR, TS, Intralayer temperature	h, w, microstructure	Low carbon steel	Ar 96%, CO_2 4%	No	3D laser lines scanner	Yes
[65]	Yes	TS	h, w	High strength steel	Ar 88%, CO_2 12%	Multiple model approach	Laser sensor	No

Table 13 (continued)

Work	CMT	Parameters	Output	Material	Gas	Model	Means of measures	ML
[66]	No	WFR, TS, CTWD	h, w	Copper coated steel	Ar 95%, CO_2 5%	Neural Network	Laser sensor	No
[67] (strut)	Yes	WFR, Arc-on time	Φ	ER 4043 aluminum	Ar	Yes (not specified)	3D profile laser scanner	No
[68]	Yes	WFR, TS, torch angle, CTWD, current, voltage, deposition direction	Q	ER70S-6; Q235	Ar 80%, CO_2 20%	No	Laser scanning	Yes
[69]	No	WFR, TS, Voltage, CTWD	h, w, p	316L stainless steel	Ar 95%, CO_2 5%	Adaptive multi-objective grey wolf algorithm	\	No

CTWD contact to work distance, *p* penetration, Φ droplet diameter, *Q* overall quality of the sample

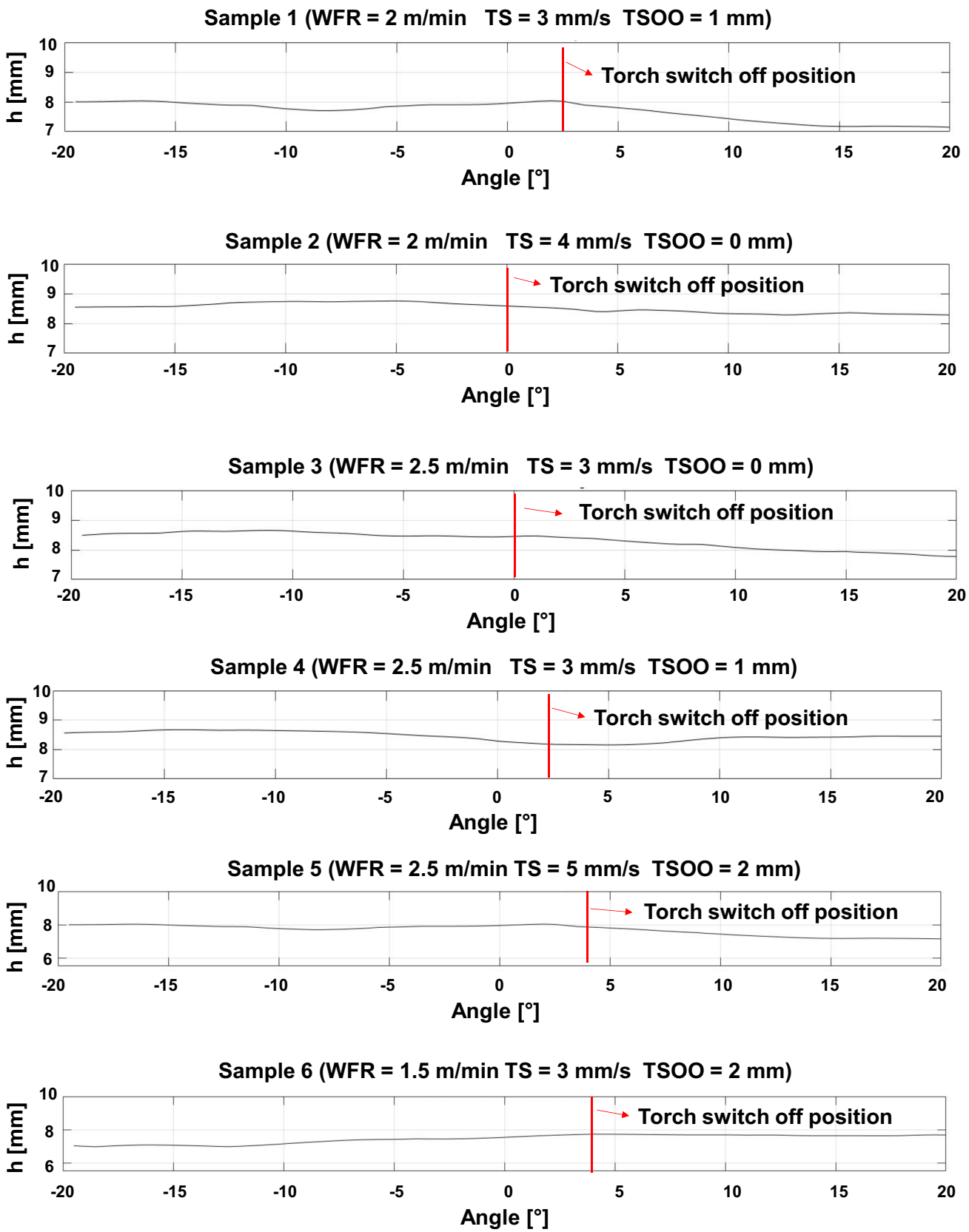

Fig. 26 Samples heights profiles in the torch switch-off zone

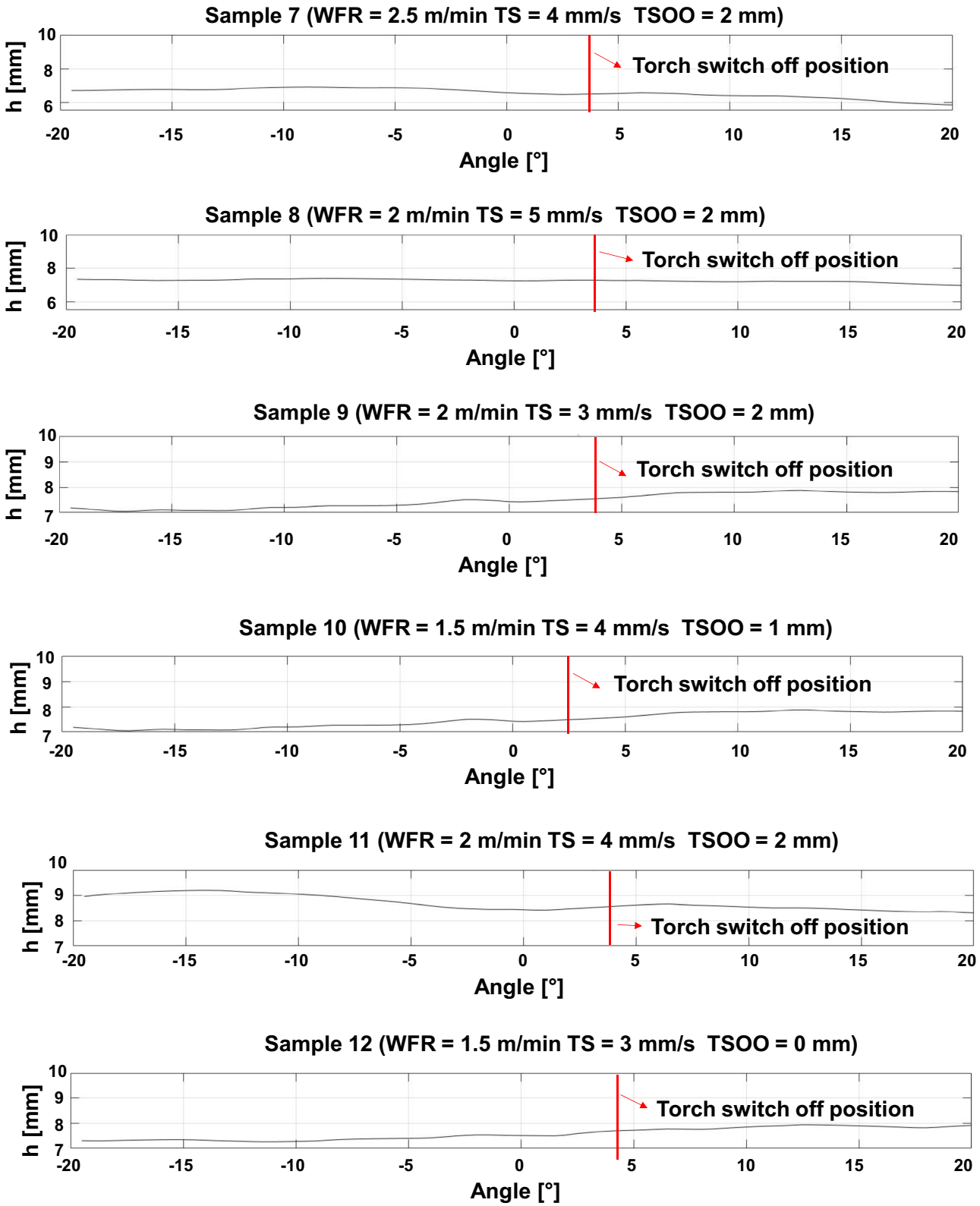

Fig. 26 (continued)

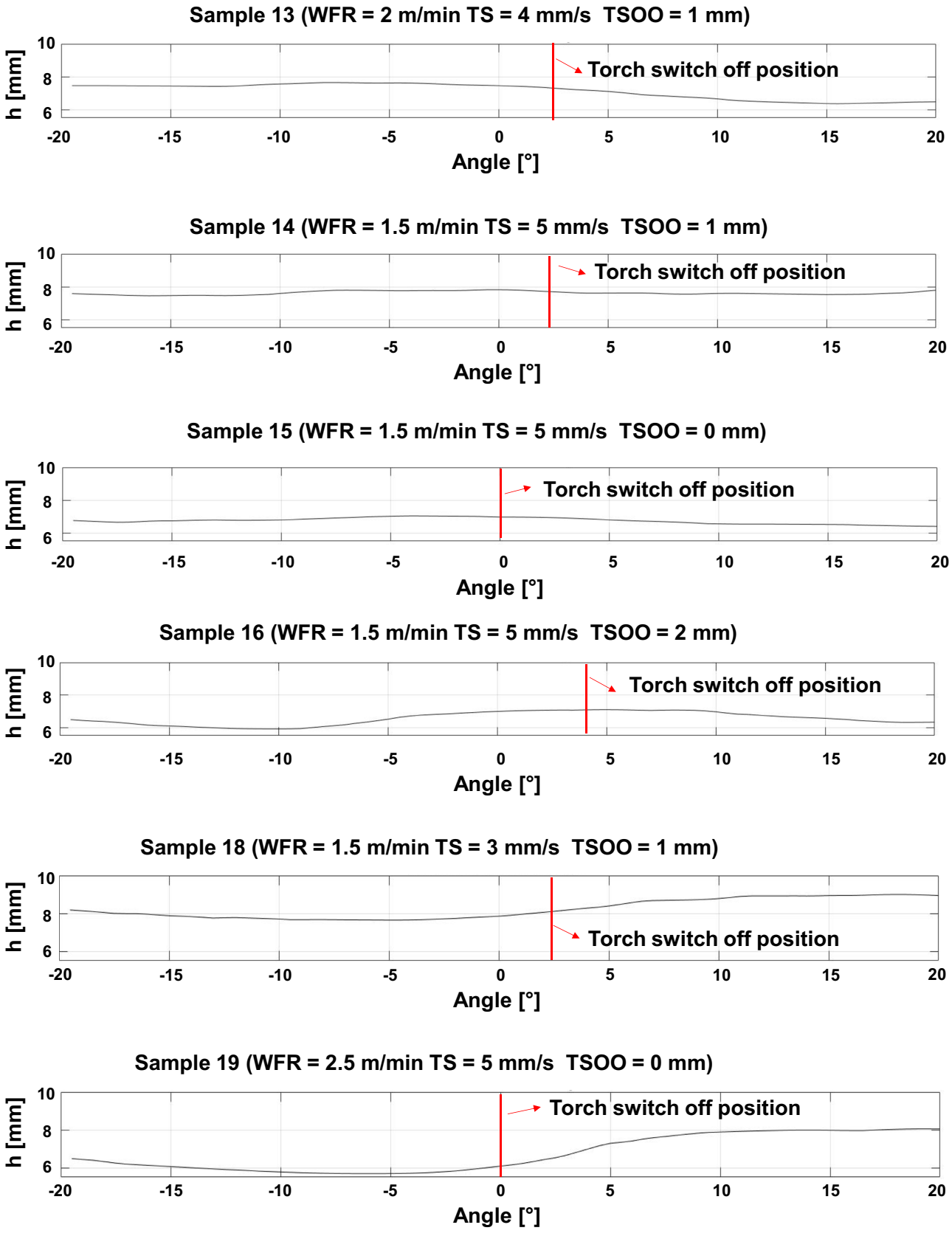

Fig. 26 (continued)

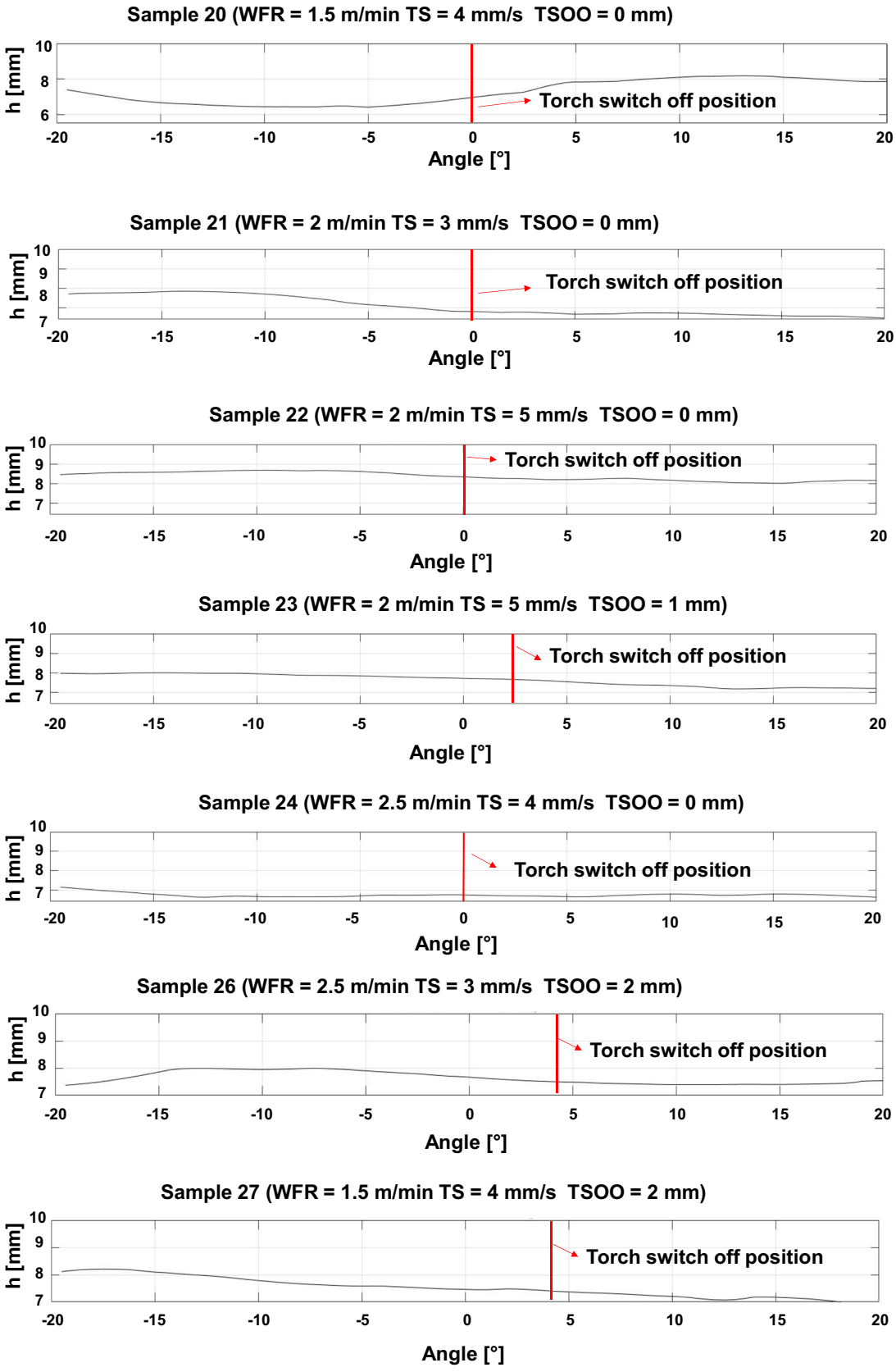

Fig. 26 (continued)

Author contribution All authors contributed to the study's conception and design. Cesare Esposto performed the experiments. Jacopo Lettori and Roberto Raffaeli worked on material preparation, data collection, and analysis. Jacopo Lettori wrote the first draft of the manuscript, Roberto Raffaeli revised the paper, and all authors commented on previous versions. All authors have read and approved the final manuscript.

Funding Open access funding provided by Università degli Studi di Modena e Reggio Emilia within the CRUI-CARE Agreement.

Data availability Not applicable.

Code availability Not applicable.

Declarations

Ethics approval Not applicable.

Consent to participate Not applicable.

Consent for publication Not applicable.

Conflict of interest The authors declare no competing interests.

References

1. Jafari D, Vaneker THJ, Gibson I (2021) Wire and arc additive manufacturing: opportunities and challenges to control the quality and accuracy of manufactured parts. Mater Des 202:109471. https://doi.org/10.1016/j.matdes.2021.109471
2. Dass A, Moridi A (2019) State of the art in directed energy deposition: from additive manufacturing to materials design. Coatings 9:418. https://doi.org/10.3390/COATINGS9070418
3. Lettori J, Raffaeli R, Bilancia P et al (2022) A review of geometry representation and processing methods for cartesian and multiaxial robot-based additive manufacturing. Int J Adv Manuf Technol 123:3767–3794. https://doi.org/10.1007/s00170-022-10432-8
4. Jiang J, Newman ST, Zhong RY (2021) A review of multiple degrees of freedom for additive manufacturing machines. Int J Comput Integr Manuf 34:195–211. https://doi.org/10.1080/0951192X.2020.1858510
5. Williams SW, Martina F, Addison AC et al (2016) Wire + arc additive manufacturing. Mater Sci Technol 32:641–647. https://doi.org/10.1179/1743284715Y.0000000073
6. Köhler M, Fiebig S, Hensel J, Dilger K (2019) Wire and arc additive manufacturing of aluminum components. Metals 9:1–9. https://doi.org/10.3390/met9050608
7. Ding D, Pan Z, Cuiuri D, Li H (2015) Wire-feed additive manufacturing of metal components: technologies, developments and future interests. Int J Adv Manuf Technol 81:465–481. https://doi.org/10.1007/s00170-015-7077-3
8. Pan Z, Ding D, Wu B, et al (2018) Arc welding processes for additive manufacturing: a review. 3–24. https://doi.org/10.1007/978-981-10-5355-9_1
9. Sadhya S, Khan AU, Kumar A et al (2024) Development of concurrent multi wire feed mechanism for WAAM-TIG to enhance process efficiency. CIRP J Manuf Sci Technol 51:313–323. https://doi.org/10.1016/j.cirpj.2024.04.010
10. Aiyiti W, Zhao W, Lu B, Tang Y (2006) Investigation of the overlapping parameters of MPAW-based rapid prototyping. Rapid Prototyp J 12:165–172. https://doi.org/10.1108/13552540610670744
11. Williams SW, Martina F (2015) Wire+arc additive manufacturing vs. traditional machining from solid: a cost comparison. Cranfield
12. Bhatt PM, Kulkarni A, Kanyuck A et al (2022) Automated process planning for conformal wire arc additive manufacturing. Int J Adv Manuf Technol 119:3545–3570. https://doi.org/10.1007/s00170-021-08391-7
13. Etienne J, Ray N, Panozzo D et al (2019) Curvislicer: slightly curved slicing for 3-axis printers. ACM Trans Graph 38:1–11. https://doi.org/10.1145/3306346.3323022
14. Zhang J, Liou F (2004) Adaptive slicing for a multi-axis laser aided manufacturing process. J Mech Des Trans ASME 126:254–261. https://doi.org/10.1115/1.1649966
15. Lettori J, Raffaeli R, Borsato M et al (2024) Implementation and virtual assessment of a non-uniform cylindrical slicing algorithm for robot-based additive manufacturing. Int J Adv Manuf Technol. https://doi.org/10.1007/s00170-024-13186-7
16. Scotti A, Ponomarev V, Lucas W (2012) A scientific application oriented classification for metal transfer modes in GMA welding. J Mater Process Technol 212:1406–1413. https://doi.org/10.1016/j.jmatprotec.2012.01.021
17. Norrish J (2009) Process control and automation developments in welding. ASM Proc Int Conf Trends Weld Res 17–24. https://doi.org/10.1361/cp2008twr017
18. Selvi S, Vishvaksenan A, Rajasekar E (2018) Cold metal transfer (CMT) technology-an overview. Def Technol 14:28–44. https://doi.org/10.1016/j.dt.2017.08.002
19. Lettori J, Raffaeli R, Borsato M, et al (2024) Empirical characterization of track dimensions for CMT-based WAAM processes. In: Silva FJG, Ferreira LP, Sà JC, et al (eds) Flexible Automation and Intelligent Manufacturing: Establishing Bridges for More Sustainable Manufacturing Systems. Springer, Cham.
20. Sampaio RFV, Pragana JPM, Bragança IMF et al (2023) Modelling of wire-arc additive manufacturing – a review. Adv Ind Manuf Eng 6. https://doi.org/10.1016/j.aime.2023.100121
21. Dinovitzer M, Chen X, Laliberte J et al (2019) Effect of wire and arc additive manufacturing (WAAM) process parameters on bead geometry and microstructure. Addit Manuf 26:138–146. https://doi.org/10.1016/j.addma.2018.12.013
22. Veiga F, Suárez A, Aldalur E, Bhujangrao T (2021) Effect of the metal transfer mode on the symmetry of bead geometry in WAAM aluminum. Symmetry 13:1245. https://doi.org/10.3390/sym13071245
23. Jorge VL, Scotti FM, Reis RP, Scotti A (2020) The potential of wire feed pulsation to influence factors that govern weld penetration in GMA welding. Int J Adv Manuf Technol 110:2685–2701. https://doi.org/10.1007/s00170-020-06037-8
24. Wang Z, Zimmer-Chevret S, Léonard F, Abba G (2022) Improvement strategy for the geometric accuracy of bead's beginning and end parts in wire-arc additive manufacturing (WAAM). Int J Adv Manuf Technol 118:2139–2151. https://doi.org/10.1007/s00170-021-08037-8
25. Venkatarao K (2021) The use of teaching-learning based optimization technique for optimizing weld bead geometry as well

as power consumption in additive manufacturing. J Clean Prod 279:123891. https://doi.org/10.1016/j.jclepro.2020.123891
26. Li Y, Dong Z, Miao J et al (2023) Forming accuracy improvement in wire arc additive manufacturing (WAAM): a review. Rapid Prototyp J 29:673–686. https://doi.org/10.1108/RPJ-05-2022-0154
27. Bigliardi M, Bilancia P, Raffaeli R, et al (2022) Path approximation strategies for robot manufacturing: a preliminary experimental evaluation. Adv Mech Des Eng Manuf IV Proc Int Jt Conf Mech Des Eng Adv Manuf JCM 2022, June 1–3, 2022, Ischia, Italy 380–389. https://doi.org/10.1007/978-3-031-15928-2_33
28. Lettori J, Raffaeli R, Borsato M et al (2024) Non-uniform planar slicing for robot-based additive manufacturing. Comput Des Appl 21:104–118. https://doi.org/10.14733/cadaps.2024.104-118
29. Abe T, Sasahara H (2019) Layer geometry control for the fabrication of lattice structures by wire and arc additive manufacturing. Addit Manuf 28:639–648. https://doi.org/10.1016/j.addma.2019.06.010
30. Ding D, Pan Z, Cuiuri D et al (2016) Bead modelling and implementation of adaptive MAT path in wire and arc additive manufacturing. Robot Comput Integr Manuf 39:32–42. https://doi.org/10.1016/j.rcim.2015.12.004
31. Nguyen L, Buhl J, Bambach M (2020) Multi-bead overlapping models for tool path generation in wire-arc additive manufacturing processes. Procedia Manuf 47:1123–1128. https://doi.org/10.1016/j.promfg.2020.04.129
32. Zhang L, Sun M, Wang H et al (2024) A layer superposition strategy based on a theoretical model for wire and arc additive manufacturing of multi-layer single-bead components. CIRP J Manuf Sci Technol 49:191–202. https://doi.org/10.1016/j.cirpj.2024.01.010
33. Yildiz AS, Davut K, Koc B, Yilmaz O (2020) Wire arc additive manufacturing of high-strength low alloy steels: study of process parameters and their influence on the bead geometry and mechanical characteristics. Int J Adv Manuf Technol 108:3391–3404. https://doi.org/10.1007/s00170-020-05482-9
34. Chen X, Su C, Wang Y et al (2018) Cold metal transfer (CMT) based wire and arc additive manufacture (WAAM) system. J Surf Investig 12:1278–1284. https://doi.org/10.1134/S102745101901004X
35. Li Y, Li X, Zhang G et al (2021) Interlayer closed-loop control of forming geometries for wire and arc additive manufacturing based on fuzzy-logic inference. J Manuf Process 63:35–47. https://doi.org/10.1016/j.jmapro.2020.04.009
36. Paul AR, Mukherjee M, Sahu MK (2023) Influence of copper interlayer on the interface characteristics of stainless steel–aluminium transitional structure in wire arc directed energy deposition. Rapid Prototyp J 1:1–14. https://doi.org/10.1108/RPJ-03-2023-0089
37. Chernovol N, Sharma A, Tjahjowidodo T et al (2021) Machinability of wire and arc additive manufactured components. CIRP J Manuf Sci Technol 35:379–389. https://doi.org/10.1016/j.cirpj.2021.06.022
38. Davis JD, Kutzer MD, Chirikjian GS (2016) Algorithms for multilayer conformal additive manufacturing. J Comput Inf Sci Eng 16:1–12. https://doi.org/10.1115/1.4033047
39. Bai R, Liang G, Cheng H, Naceur H, Coutellier D, Zhao J, Luo J, Pu H, Yi J (2023) Optimizing additive manufacturing path pattern for Ti-6Al-4V thin rods using a combinatorial radial basis function surrogate-assisted genetic algorithm. Mater Des 236:112447. https://doi.org/10.1016/j.matdes.2023.112447
40. Bai R, Shi S, Wang J, Luo J, Pu H, Lyu W, Naceur H, Coutellier D, Wang L, Du Y (2024) Investigation of printing turn angle effects on structural deformation and stress in selective laser melting. Mater Des 247:113347. https://doi.org/10.1016/j.matdes.2024.113347
41. Guo H, Hu J, Tsai HL (2009) Formation of weld crater in GMAW of aluminum alloys. Int J Heat Mass Transf 52:5533–5546. https://doi.org/10.1016/j.ijheatmasstransfer.2009.06.028
42. Derrien R, Sullivan EM, Liu S et al (2021) Silicate island formation in gas metal arc welding. Weld J 100:13–26. https://doi.org/10.29391/2021.100.002
43. Germani M, Raffaeli R, Mazzoli A (2010) A method for performance evaluation of RE/RP systems in dentistry. Rapid Prototyp J 16:345–355. https://doi.org/10.1108/13552541011065740
44. Comotti C, Regazzoni D, Rizzi C, Vitali A (2017) Additive manufacturing to advance functional design: an application in the medical field. J Comput Inf Sci Eng 17:031006. https://doi.org/10.1115/1.4033994
45. Dean A, Voss D (1999) Design and analysis of experiments. Springer
46. Miller RG Jr (1997) Beyond ANOVA: basics of applied statistics. Routledge
47. Antony J (2014) A systematic methodology for design of experiments. Des Exp Eng Sci 2:33–50
48. Evans SI, Wang J, Qin J et al (2022) A review of WAAM for steel construction – manufacturing, material and geometric properties, design, and future directions. Structures 44:1506–1522. https://doi.org/10.1016/j.istruc.2022.08.084
49. Busachi A, Erkoyuncu J, Colegrove P et al (2015) Designing a WAAM based manufacturing system for defence applications. Procedia CIRP 37:48–53. https://doi.org/10.1016/j.procir.2015.08.085
50. Cheng J, De Waele W (2024) Prediction and optimization of surface waviness of WAAM components using a hybrid Rank-Gaussian PSO algorithm and ANN. Structures 69:107247. https://doi.org/10.1016/j.istruc.2024.107247
51. Pattanayak S, Sahoo SK (2023) Effect of travel speed and number of layers on surface waviness of ER70S6 deposits fabricated through non-transferred wire arc additive manufacturing. J Adhes Sci Technol 37(24):3622–3651. https://doi.org/10.1080/01694243.2023.2217541
52. Ozaner OC, Talemi R, Tjahjowidodo T, Sharma A (2024) The influence of the wire and arc additive manufacturing parameters on the surface irregularities. J Micromanuf. https://doi.org/10.1177/25165984241306629
53. Bai R, Pu H, Liang G, Naceur H, Coutellier D, Du Y, Zhao J, Yi J, Li X, Yuan S, Luo J, Lin J (2024) Exact forming for additive manufacturing using an irregular element-based compensating approach: simulation, experiment, and detection. Mech Adv Mater Struct 31(26):7567–7578. https://doi.org/10.1080/15376494.2023.2246191
54. Ding D, Pan Z, Cuiuri D, Li H (2015) A multi-bead overlapping model for robotic wire and arc additive manufacturing (WAAM). Robot Comput Integr Manuf 31:101–110. https://doi.org/10.1016/j.rcim.2014.08.008
55. Karmuhilan M, Sood AK (2018) Intelligent process model for bead geometry prediction in WAAM. Mater Today Proc 5:24005–24013. https://doi.org/10.1016/j.matpr.2018.10.193
56. Lambiase F, Scipioni SI, Paoletti A (2022) Accurate prediction of the bead geometry in wire arc additive manufacturing process. Int J Adv Manuf Technol 119:7629–7639. https://doi.org/10.1007/s00170-021-08588-w
57. Le VT, Doan QT, Mai DS et al (2022) Prediction and optimization of processing parameters in wire and arc-based additively manufacturing of 316L stainless steel. J Brazilian Soc Mech Sci Eng 44:1–16. https://doi.org/10.1007/s40430-022-03698-2
58. Li F, Chen S, Shi J et al (2017) Evaluation and optimization of a hybrid manufacturing process combining wire arc additive manufacturing with milling for the fabrication of stiffened panels. Appl Sci 7:1233. https://doi.org/10.3390/app7121233

59. Li F, Chen S, Shi J et al (2018) Thermoelectric cooling-aided bead geometry regulation in wire and arc-based additive manufacturing of thin-walled structures. Appl Sci 8. https://doi.org/10.3390/app8020207
60. Novelino ALB, Carvalho GC, Ziberov M (2022) Influence of WAAM-CMT deposition parameters on wall geometry. Adv Ind Manuf Eng 5. https://doi.org/10.1016/j.aime.2022.100105
61. Panda B, Shankhwar K, Garg A, Savalani MM (2019) Evaluation of genetic programming-based models for simulating bead dimensions in wire and arc additive manufacturing. J Intell Manuf 30:809–820. https://doi.org/10.1007/s10845-016-1282-2
62. Tang S, Wang G, Song H et al (2021) A novel method of bead modeling and control for wire and arc additive manufacturing. Rapid Prototyp J 27:311–320. https://doi.org/10.1108/RPJ-05-2020-0097
63. Teixeira FR, Scotti FM, Jorge VL, Scotti A (2023) Combined effect of the interlayer temperature with travel speed on features of thin wall WAAM under two cooling approaches. Int J Adv Manuf Technol 126:273–289. https://doi.org/10.1007/s00170-023-11105-w
64. Wang Z, Zimmer-Chevret S, Léonard F, Abba G (2022) Control of bead geometry using multiple model approach in wire-arc additive manufacturing (WAAM). Int J Adv Manuf Technol 122:2939–2951. https://doi.org/10.1007/s00170-022-10053-1
65. Xiong J, Zhang G, Gao H, Wu L (2013) Modeling of bead section profile and overlapping beads with experimental validation for robotic GMAW-based rapid manufacturing. Robot Comput Integr Manuf 29:417–423. https://doi.org/10.1016/j.rcim.2012.09.011
66. Yu Z, Ding D, Pan Z et al (2021) A strut-based process planning method for wire arc additive manufacturing of lattice structures. J Manuf Process 65:283–298. https://doi.org/10.1016/j.jmapro.2021.03.038
67. Yuan L, Pan Z, Ding D et al (2021) Fabrication of metallic parts with overhanging structures using the robotic wire arc additive manufacturing. J Manuf Process 63:24–34. https://doi.org/10.1016/j.jmapro.2020.03.018
68. Zhao Y, Li W, Liu A (2020) Optimization of geometry quality model for wire and arc additive manufacture based on adaptive multi-objective grey wolf algorithm. Soft Comput 24:17401–17416. https://doi.org/10.1007/s00500-020-05027-y
69. Couto MO, Rodrigues AG, Coutinho F et al (2022) Mapping of bead geometry in wire arc additive manufacturing systems using passive vision. J Control Autom Electr Syst 33(4):1136–47